EDGEWOOD CHEMICAL BIOLOGICAL CENTER
U.S. ARMY RESEARCH, DEVELOPMENT AND ENGINEERING COMMAND
Aberdeen Proving Ground, MD 21010-5424

ECBC-TR-1565

RAPID DETECTION OF DRUGS AND EXPLOSIVES FOR FORENSIC ANALYSIS

Carl D. Meinhart
Martin Moskovits

UNIVERSITY OF CALIFORNIA, SANTA BARBARA
Santa Barbara, CA 93106-0001

Neal D. Kline
Augustus Way Fountain III

RESEARCH AND TECHNOLOGY DIRECTORATE

December 2018

U.S. ARMY RDECOM

Disclaimer

The findings in this report are not to be construed as an official
Department of the Army position unless so designated by other authorizing documents.

REPORT DOCUMENTATION PAGE

Form Approved
OMB No. 0704-0188

1. REPORT DATE *(DD-MM-YYYY)*	**2. REPORT TYPE**	**3. DATES COVERED** *(From - To)*
XX-12-2018	Final	Oct 2014 – Mar 2018

4. TITLE AND SUBTITLE
Rapid Detection of Drugs and Explosives for Forensic Analysis

5a. CONTRACT NUMBER
W911NF-09 D-0001

5b. GRANT NUMBER

5c. PROGRAM ELEMENT NUMBER

6. AUTHOR(S)
Meinhart; Carl D.; Moskovits, Martin (UCSB); Kline, Neal D.; Fountain, Augustus Way III (ECBC)

5e. TASK NUMBER
0039

5f. WORK UNIT NUMBER

7. PERFORMING ORGANIZATION NAME(S) AND ADDRESS(ES)
University of California, Santa Barbara, 552 University Road, Santa Barbara, CA 93106-001
Director, ECBC, ATTN: RDCB-DR, APG, MD 21010

8. PERFORMING ORGANIZATION REPORT NUMBER
ECBC-TR-1565

9. SPONSORING / MONITORING AGENCY NAME(S) AND ADDRESS(ES)

10. SPONSOR/MONITOR'S ACRONYM(S)

11. SPONSOR/MONITOR'S REPORT NUMBER(S)

12. DISTRIBUTION / AVAILABILITY STATEMENT
Approved for public release: distribution unlimited.

13. SUPPLEMENTARY NOTES

14. ABSTRACT:
We developed an approach based upon microfluidics and SERS that can detect drugs of abuse and explosives, as well as other molecules of interest for forensic analysis at ultra-low concentrations and with measurement times of a few minutes. The resulting approach will be applicable to field-portable and handheld surface-enhanced Raman instruments.

15. SUBJECT TERMS
Surface-Enhanced Raman Spectroscopy
Microfluidics

16. SECURITY CLASSIFICATION OF:			**17. LIMITATION OF ABSTRACT**	**18. NUMBER OF PAGES**	**19a. NAME OF RESPONSIBLE PERSON**
a. REPORT	**b. ABSTRACT**	**c. THIS PAGE**			Renu B. Rastogi
U	U	U	UU	48	**19b. TELEPHONE NUMBER** *(include area code)* (410) 436-7545

Blank

PREFACE

The work described in this report was authorized under contract number W911NF-09 D-0001 and task number 0039. The work was started in October 2014 and completed in March 2018

The use of either trade or manufacturers' names in this report does not constitute an official endorsement of any commercial products. This report may not be cited for purposes of advertisement.

The text of this report is published as received and was not edited by the Technical Releases Office, U.S. Army Edgewood Chemical Biological Center.

This report has been approved for public release.

Acknowledgments

The authors acknowledge the following individuals for their hard work and assistance with the execution of this technical program:

Rustin Mirsafavi and Reza Salemmilani (University of California, Santa Barbara; Santa Barbara, CA) for conducting experiments.

Blank

EXECUTIVE SUMMARY

We developed an approach based upon microfluidics and surface-enhanced Raman spectroscopy (SERS) that can detect drugs of abuse and explosives, as well as other molecules of interest for forensic analysis at ultra-low concentrations and with measurement times of a few minutes. The resulting approach will be applicable to field-portable and handheld surface-enhanced Raman instruments.

Papaverine is a non-narcotic alkaloid found endemically and uniquely in the latex of the opium poppy. It is normally refined out of the opioids that the latex is normally collected for, hence its presence in a sample is strong *prima facie* evidence that the carrier from whom the sample was collected is implicated in the mass cultivation of poppies or the collection and handling of their latex. We developed an analysis technique combining SERS with microfluidics for detecting papaverine at low concentrations and show that its SERS spectrum has unique spectroscopic features that allows its detection at low concentrations among typical opioids. The analysis required approximately 2.5 minutes to complete, which is compatible with field use. The weak acid properties of papaverine hydrochloride were investigated, and Raman bands belonging to the protonated and unprotonated forms of the isoquinoline ring of papaverine were identified.

We developed a microfluidics-based dielectrophoresis-SERS device, which is capable of detecting physiologically relevant concentrations of methamphetamine in saliva in under two minutes. In this device, iodide-modified silver nanoparticles are trapped and released on-demand using electrodes integrated in a microfluidic channel. Principal component analysis is used to reliably distinguish methamphetamine-positive samples from the negative control samples. Passivation of the electrodes and flow channels minimizes microchannel fouling by nanoparticles, which allows the device to be cleared and reused multiple times.

We developed a quantitative analysis strategy with which low concentrations of three analytes (cocaine, methamphetamine, and papaverine) can be determined using SERS analysis, with citrate functioning as an *in situ* standard. The silver nanoparticles are initially saturated with citrate as a capping agent that is subsequently displaced by the analyte to an extent dependent on the analyte's concentration in the analyte solution. We developed a quantitative adsorption model through which the relative SERS intensity of the analyte and citrate remaining on the silver's surface can be directly related to the analyte's concentration in solution. By carrying out the analyses in a microfluidic channel, SERS spectra can be recorded corresponding to known exposure times of the silver nanoparticles to the analyte. This allows one to determine the relative surface concentrations of the analyte and citrate as a function of time, showing convincingly that the analyte adsorbs on the silver by displacing citrate. Classical least squares analysis is used to determine confidently the relative SERS signal intensities corresponding to the citrate and the analyte.

While silver and gold have been the dominant plasmonic metals used for SERS since the field's inception, our results suggest that virtually any appropriately nanostructured material with sufficiently high electrical conductivity has the potential to be an efficient SERS substrate. Metals with advantages over silver and gold such as high natural abundance, low cost,

and useful catalytic activity could be used as the basis for SERS substrates. Using our nanofabrication scheme for creating large-format SERS substrates, we produced highly performing SERS substrates using aluminum and nickel, in addition to copper, silver, and gold as benchmarks. All five metals are found to yield high SERS intensities. Their relative SERS enhancement is ascribed mainly to local field effects, with the grating-based enhancement making an approximately equivalent contribution to the SERS enhancement for the five metals. This conclusion is also supported by local electric field simulations.

CONTENTS

FIGURES

Blank

RAPID DETECTION OF DRUGS AND EXPLOSIVES FOR FORENSIC ANALYSIS

1. INTRODUCTION

The opium poppy (*Papaver somniferum*) has been cultivated for its analgesic and narcotic properties since pre-historic times.[1] The sap, or latex, of the poppy plant—when dried to yield opium—contains multiple alkaloids including morphine, thebaine, codeine, papaverine, and noscapine (see Figure 1). While opium is the source for the active ingredients of several pain-relieving pharmaceuticals such as morphine, codeine, and hydrocodone, it is also the source of heroin—a highly addictive, illicit substance. Opiate addiction is a serious medical and social problem, with significant harmful economic consequences;[2] and the opium trade is a serious global criminal enterprise, some of whose profits also fund international terrorist activities.[3] Moreover, despite massive national and international policing efforts, those who traffic in opiates routinely find new ways to move these substances across borders. Developing the analytical means for credibly identifying the people responsible for the early stages of this complex trade—those who grow, harvest and obtain the latex from the poppy—could, therefore, be useful in reducing opiate trafficking.

Most chemical detection methods for opiates, such as gas chromatography and/or mass spectrometry, understandably and valuably focus on opiates. That approach, however, does not distinguish the illicit user or trafficker from individuals involved in the cultivation of poppies or the refinement of its latex, i.e., the individuals closest to the source. Here we propose the molecule papaverine as an analyte that occurs exclusively in the opium poppy. Although it is not itself a narcotic, and occurs at negligible concentrations in the finished opiate, its presence on skin or clothes would be *prima facie* evidence that the individual so identified had handled opium poppies or their latex. Below we describe a sensing technique based on combining surface-enhanced Raman spectroscopy (SERS) with microfluidics as a rapid and discriminating sensor for papaverine implicating, *prima facie*, the individual from whom the sample was obtained in the large-scale cultivation of poppies and/or in handling its latex.

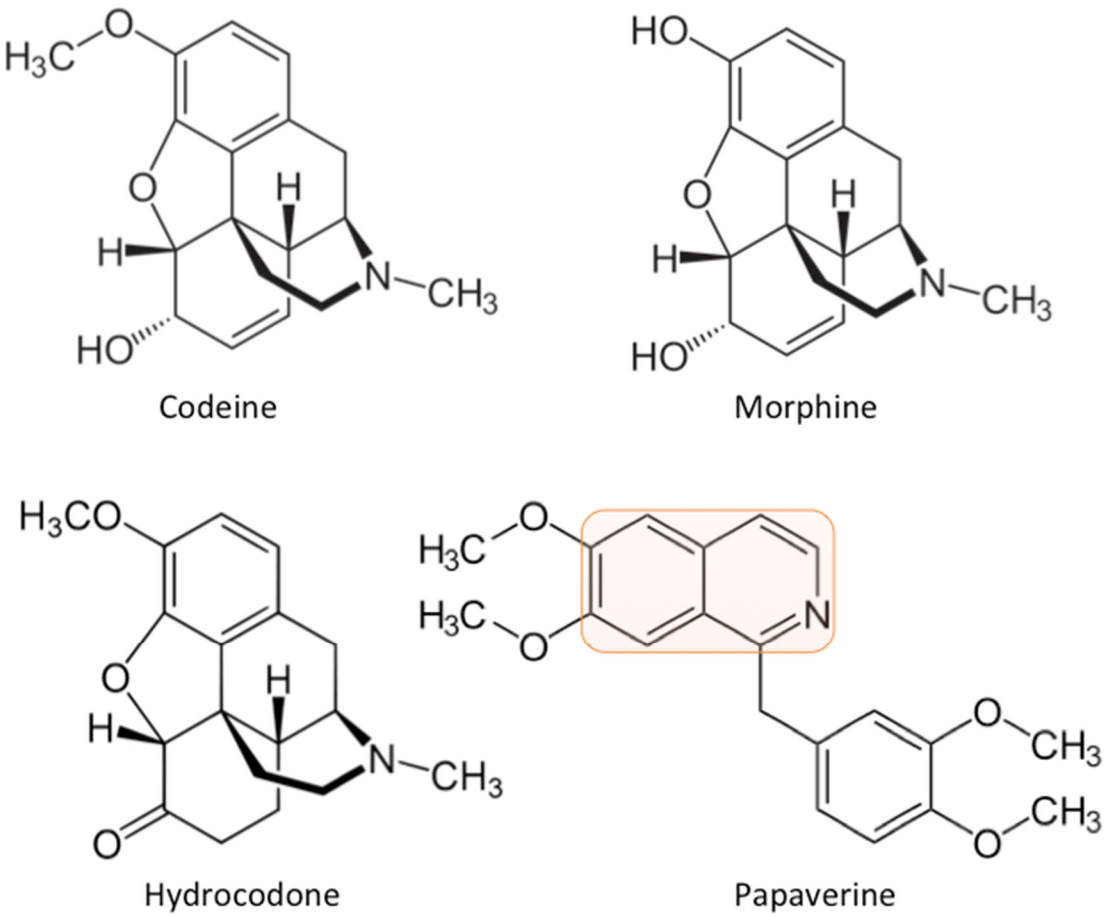

Figure 1. Molecular structures of four of the alkaloids commonly found in the latex of the poppy plant. A major difference distinguishing papaverine from the opioids is the presence of an isoquinoline ring (highlighted) which produces a characteristic Raman signature. The nitrogen on the isoquinoline is the locus of papaverine's weak acidic properties.

The widespread use of illicit drugs is a major contributor to the costs of law enforcement, healthcare, and lost workforce productivity.[4] A fast and low-cost clinical and forensic screening assay would be a valuable tool in healthcare and law enforcement. Ideally, such an assay should be sensitive, specific, rapid, inexpensive, noninvasive, field-deployable, and capable of accommodating biological fluids with minimal processing.[5] Current screening techniques often rely on colorimetry for analysis, which typically only identifies classes of drugs. Moreover, as a single-parameter visual test, colorimetry is limited by subjective color perception. Consequently, a positive colorimetric test result often requires validation by more sensitive and specific laboratory techniques such as gas chromatography-mass spectroscopy (GC-MS), high-performance liquid chromatography-mass spectroscopy (HPLC-MS), etc.

SERS is a vibrational spectroscopy technique that employs surface plasmon resonance to enhance the Raman scattering from analyte molecules. Metallic nanostructures that are capable of sustaining localized surface plasmon resonances (LSPR) are normally used as

substrates for SERS.[6] Examples of such substrates are nanowires, nanoshells, and nanoparticle aggregates.[7–10] Enhancement factors can be as high as 10^8 and potentially capable of single molecule detection.[11,12] A clear advantage of SERS over colorimetric techniques is its ability to yield a molecule-specific vibrational spectrum, eliminating in many cases the need for analyte-specific reagents and multiple test kits. Due to the naturally small size of the nanoscale substrates, SERS-based chemical detection platforms are amenable to miniaturization and can be used for label-free multi-analyte detection. Chip-based SERS devices have been used to detect trace concentrations of illicit drugs, explosives, cancer biomarkers, and other classes of molecules.[13–16]

Various biological fluids such as saliva, blood plasma, urine, and sweat are typically used as matrices for drug testing.[17–19] Urine is the most common medium; however, saliva has several advantages. Unlike urine, saliva collection is considered noninvasive and potentially applicable in road-side drug testing. Its collection minimizes sample adulteration risk by direct supervision at the time of sample collection. Moreover, parent drugs are often detectable in saliva, while urine testing mainly quantifies drug metabolites of the target substance. Most importantly, detection and quantification of parent drugs in saliva can be good indicators of the level of impairment.[20]

Here we report a microfluidic chip-based SERS platform that employs dielectrophoresis (DEP) for highly localized trapping and release of SERS-active nanoparticles, on demand. The platform creates a pristine SERS substrate prior to each measurement, enabling rapid detection of physiologically relevant concentrations of methamphetamine. Since the detection mechanism is based on DEP actuation to form the SERS-hot substrate for detection, the microfluidic chip can be reliably reused over multiple cycles in which the device is cleared and a new sample is introduced. This type of on-demand aggregation system could be field deployed, in circumstances requiring high sensitivity and quick response times.

DEP refers to migration of polarizable particles in electric field gradients. DEP has been extensively used in microfluidic devices for manipulation, sorting, and trapping of particles and cells. DEP theory and its applications in microfluidic technology have been extensively reviewed.[21–23] Microfluidic-based DEP has been combined with SERS for characterizing WO_3 and polystyrene nanoparticles.[24] Chrimes *et al.* have reported controlled aggregation of silver nanoparticles in a microfluidic platform and subsequent detection of 1 ppm dipicolinic acid in DI water using SERS.[25] The same authors also used microfluidic DEP and SERS to capture and probe silver nanoparticle-coated yeast cells.[26] Cherukulappurah *et al.* have reported dielectrophoresis-enabled assembly of metallic nanoparticles using microfabricated interdigitated electrodes for detecting benzenethiol using SERS. SERS-active nanoparticle aggregates were produced by DEP which, together with analyte, were drop-cast onto the electrodes. This technique was further extended for detecting adenine.[27] Microfluidic-based DEP has also been used to trap bacteria with subsequent chemical analysis and identification using SERS.[28–30] More recently an insulator-dielectrophoresis-based microfluidic device has been reported for detection of crystal violet using SERS.[31] In the current study, we report the use of a DEP-SERS platform as a reusable probe for detecting drugs of abuse in saliva.

Our device comprises a polydimethylsiloxane (PDMS) microchannel sandwiched between an electrode substrate and a top cover. Fluid flow is established with negative pressure by applying vacuum to the outlet of the channel. An AC electric potential is applied to the electrode contact pads to activate the DEP nanoparticle trap. Silver nanoparticles, premixed with the analyte, agglomerate in the trap region to form SERS 'hotspots'. Spectra are then acquired by scanning the trap regions using a Raman microscope.

Precise determination of the concentration of narcotic drugs in a sample is pertinent to our understanding, control, and policing of drug use, trafficking, and production. Many techniques are available for determining the presence of such substances either directly, or indirectly by determining, for example, drug metabolites or residues. When choosing between a direct or indirect analytical target, the capabilities of the analytical system must roughly match the anticipated results, which normally means determining the identity of the drug and its concentration. SERS has been shown to be capable of identifying a wide range of molecules at low concentrations.[32–38]

Nanostructured metals are commonly used as SERS substrates on which such measurements are carried out. These have been produced in a variety of forms such as colloidal nanoparticles, fixed nanoparticles, and nanofabricated substrates.[39,40] Colloidal metal nanoparticles are the most prevalent materials used to detect SERS signals. In colloidal nanoparticle systems, a large fraction of the SERS signal normally arises from nanoparticle aggregates in which the interstices function as so-called SERS "hot spots" where the enhanced optical fields and, consequently, the SERS signals from molecules occupying such hot spots are thought to be especially intense.[41] The formation of aggregates is often induced by an aggregating agent that disrupts the electrostatic repulsive forces responsible for nanoparticle's stability in solvents. When using silver nanoparticles (AgNP), a common capping agent that stabilizes the colloid is citrate, a remnant of the reduction process through which the silver colloid was synthesized.[42,43] Citrate-capped AgNP are the most common type of commercial AgNPs available. These are particularly useful for SERS applications because citrate anions, unlike capping agents such as polyvinylpyrrolidone (PVP), are displaced by a wide range of analytes. However, citrate produces intense and potentially interfering SERS signals of its own and is not fully displaced by many analytes, attaining, instead, a surface equilibrium with the analyte. One of the key points we demonstrate in this study is that such analyte/citrate surface equilibria can be used as a calibration technique for producing trustworthy analyte calibration curves by correlating relative analyte to citrate SERS intensities to analyte concentration.

Additionally, the microfluidic device used exploits the diffusion-dominated laminar flow regime providing ample time for the analyte/citrate surface equilibrium to be attained before the SERS analysis is carried out downstream in the channel. Limits of detection using this microfluidic device are determined for the analytes methamphetamine, papaverine, and cocaine. Classical least squares (CLS) chemometrics are used to quantify the relative contributions of analyte and citrate. Finally, a surface kinetics model is constructed on the basis of which a reliable calibration curve is computed for each of the three analytes, relating the analyte and citrate SERS signal intensities to the analyte concentration.

2. PAPAVERINE DETECTION

2.1 Experimental Approach

The flow-focusing microfluidic device was designed with three channels that merge at a junction at which analyte (middle channel), aqueous AgNPs, and LiCl solution (side channels) join, thereafter creating interfaces across which molecular species can diffuse (as shown in Figure 2). The fluid velocity magnitude is shown in Figure 2, which was estimated from numerical simulation of the Navier-Stokes equations using *COMSOL Multiphysics V5.2* (Stockholm, Se). The red color represents a maximum velocity magnitude of approximately 1 mm/s. The solid black lines indicate the streamlines emanating from the analye channel. At the channel cross-section, the black streamlines become focused towards the center of the channel. This design and its operation were previously described. Briefly, the AgNPs diffuse little on account of their size and mass, while the analyte in the middle channel diffuse into the silver colloid stream adsorbing on the nanoparticles. The LiCl, that acts as an AgNP aggregating agent, must diffuse across the middle channel before encountering the (now analyte-covered) nanoparticles, causing them to form aggregates that produce intense SERS signals. The microfluidic flow is induced by a vacuum system applied to the outlet. The relative rates of flow in the respective channels are managed by serpentine channels. The microfluidic device was fabricated using previously-described microelectromechanical systems (MEMS)-based lithographic processes.[44] Briefly, a mold was created on a 4-inch silicon wafer using SU-8 photoresist. PDMS (Sylgard 184, Dow Corning®) was cast upon the mold and peeled off to yield microchannels. The PDMS pieces containing the microchannels were sealed with 200 µm-thick Pyrex® microscope cover slips (Fisher Scientific™). Both PDMS and glass were ozonated (UVO-Cleaner® 42, Jelight Company Inc.) prior to bonding to create a robust and permanent seal.

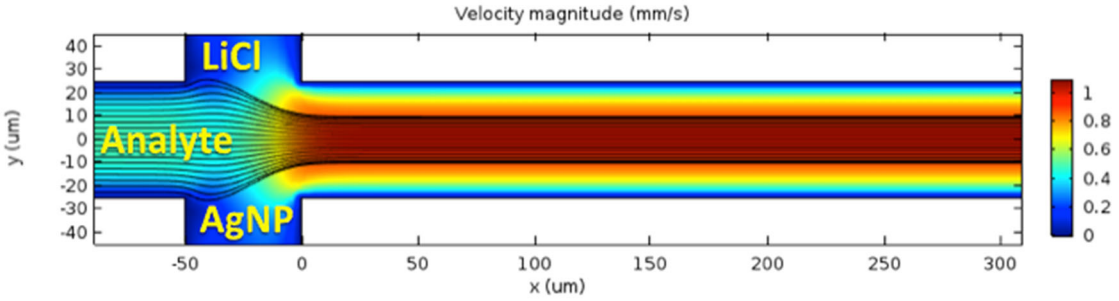

Figure 2. Simulation of the hydrodynamics in the flow-merging device showing velocity lines of fluid flow. Laminar flow is achieved resulting in diffusion-dominated processes that cause the analyte and the lithium chloride to cross sequentially into the stream containing the AgNPs, the former leading to analyte adsorption; the latter causing AgNP aggregation.

Approximately 20 nm dia. citrate-capped AgNPs (nanoComposix, product: AGCB20-1M) in colloidal suspension were diluted 1:100 from 1 mg/mL stock solution. A concentrated papaverine HCl (MP Biomedicals, SKU: 02190261) solution was prepared by dissolving as much papaverine as would dissolve in room temperature DI water, which produces a solution of approximately 40 mM. From this stock solution, papaverine HCl solutions of 1000 ppm, 100 ppm, 10 ppm, 5 ppm, and 2 ppm, corresponding to 3000 µM, 300 µM, 30 µM,

15 μM, and 6 μM, respectively, were prepared. Because the solution was produced from the HCl salt of papaverine, the concentration of free base papaverine in solution is approximately 2 % lower than the nominal values. Also, the HCl salt releases H^+ when dissolved, producing solution of varying pH as a function of the papaverine HCl concentration such that solutions with concentrations of 3000 μM, 300 μM, 30 μM, 15 μM, and 6 μM had measured pH values of 4.23, 4.95, 5.44, 5.60, and 5.66, respectively. (We show below, that these values suggest a pK_a value of 6.0 for papaverine HCl, which agrees with an estimated pK_a value of 6.03 (ChemAxon)for papaverine HCl, but disagrees with other reported values.[5] An ionic solution of 0.2 M LiCl was used as aggregating agent for all solutions except for those with concentrations of 3000 μM and 300 μM, which were found to produce a great deal of AgNP aggregation on their own, presumably on account of the "high" concentration of Cl^- ions originating from the papaverine salt.

Spectra were collected using a confocal micro-Raman system (LabRAM ARAMIS spectrometer (HORIBA, Ltd., Kyoto, JP)), with 0.87 mW of 633 nm laser and 1 s acquisition time per point while the device was under flow. An optimal interrogation area of 60 μm x 250 μm located 100 μm downstream from the junction was found for all concentrations of analyte. This interrogation scheme proved to be an optimal region for SERS signal and also allowed for quick generation of data (within 2.5 min) by rasterization of the region in the microchannel.

2.2 Papaverine Detection Results

Various reference and control spectra were measured. Flowing DI H_2O through the center ("analyte") channel produced spectra that contained only PDMS Raman bands. Raman spectra of solid papaverine HCl powder and concentrated papaverine HCl dissolved in a AgNP solution agreed well with each other as well as with previously-reported Raman spectra. For example, Figure 3 shows the Raman spectrum of 40 mM papaverine HCl dissolved in a 1:1 ratio with 0.1 mg/mL AgNP solution.). A droplet of the solution was placed on a glass slide and was interrogated at a single point with a 633 laser at 3.8 mW laser power for 1 second. While the SERS peaks are consistent with those measured for the various concentrations of papaverine HCl, this reference sample produced a spectrum approximately twenty times more intense than what we measured for the 3,000 μM solution flowed in the device. Such a large difference in intensity was due the reference solution being much more concentrated as well as the necessary attenuation of the laser power in the device, as papaverine decomposes under high laser powers. Analysis of the raw spectra shown in Figure 3 involved the averaging of counts from different device runs at the same concentration of analyte as well as the normalization of each spectra to the intensity of the most intense band for a given concentration.

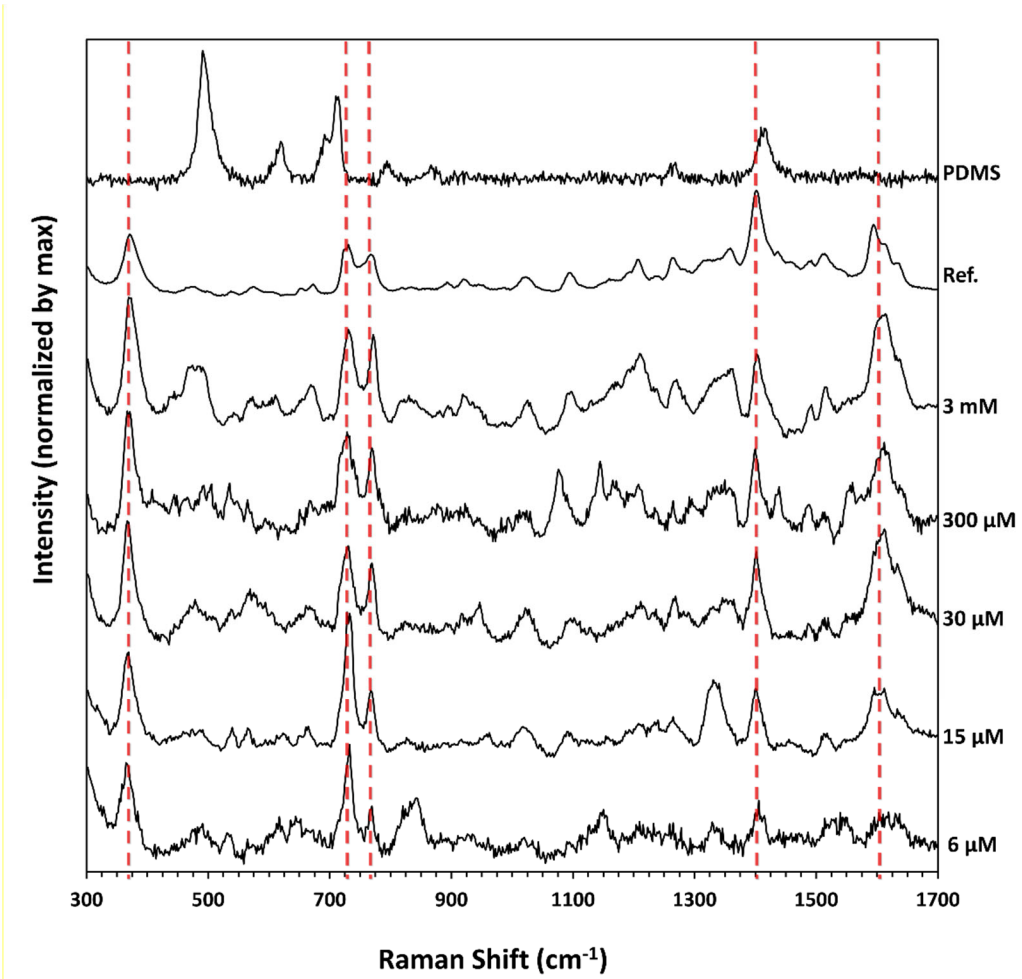

Figure 3. SERS spectra obtained of aqueous papaverine HCl solutions of the indicated concentrations. Other than the reference spectrum (Ref.) the SERS spectra presented were collected from the microfluidic flow-merging device using identical interrogation and collection schemes. The red dashed lines indicate the Raman shifts that reoccur reproducibly in all of the spectra and are assigned to papaverine. The spectra shown are averaged and each normalized to the intensity of the most intense band in the spectrum.

Although the SERS experiments were carried out in a PDMS device, the Raman peaks of PDMS were normally much weaker than the intensities of the most intense papaverine SERS bands, for example, those at 369 cm^{-1}, 730 cm^{-1}, 769 cm^{-1}, 1401 cm^{-1}, and 1614 cm^{-1}. These correspond well with previously reported and assigned papaverine bands. Many of these are also easily distinguished from known features in the spectra of opiates such as morphine, codeine, and hydrocodone (see Figure 4) allowing one to detect papaverine in the presence of other components of the latex which would also likely be present in samples collected from a suspected poppy or latex handler. Peaks near 1614 cm^{-1} and 1401 cm^{-1} also occur in the spectra of opiates and have been assigned to various phenyl ring stretching modes, while the peaks at 369 cm^{-1}, 730 cm^{-1}, and 769 cm^{-1} do not occur in opiates. The single peak at 369 cm^{-1} and the doublet peak at 730 cm^{-1} and 769 cm^{-1} have both been previously assigned to modes associated with the isoquinoline ring in papaverine.

The relative intensities of some SERS papaverine bands associated with its isoquinoline ring appear to be dependent on the analyte's concentration. We ascribe this to the varying ratio of the protonated and deprotonated forms of papaverine due to the change in solution pH with varying analyte concentration (the higher the concentration, the lower the pH). Specifically, the intensity ratio of the peaks at 730 cm^{-1} and 769 cm^{-1} vary systematically as the papaverine concentration is varied. The area of each of the two overlapping SERS bands was determined as a function of pH by fitting a Lorentzian to each of the overlapping SERS features. We find (Figure 3) that the ratio of the 730 cm^{-1} to 769 cm^{-1} band intensities increases as the concentration of papaverine decreases, implying that the 730 cm^{-1} band belongs to the deprotonated form of the papaverine, and implies that papaverine behaves as a weak acid.

A straight-forward weak acid analysis was carried out (reported in detail in the Supporting Information) which yielded a calculated pH value at each value of concentration assuming various parametric values of pKa. A selection of the results is shown in Figure 4, where we show that the measured pH values of papaverine HCl dissolved in DI water agrees well with what we calculate assuming $pK_a = 6$.This accords with one of the previously estimated pK_a values for papaverine HCl, (ChemAxon) but contrasts with other reports.[5]

The aforementioned 730 cm^{-1} to 769 cm^{-1} band intensity ratio, is shown in the Supporting Information section to depend on pH and as

$$Log_{10}\frac{S_{PH+}}{S_P} = Log_{10}\frac{[\sigma_P]}{[\sigma_{PH+}]} - Log_{10}K_a + pH, \quad (1)$$

in which S_{PH+}, S_P, σ_{PH+} and σ_P, respectively, are the SERS intensities of the protonated and deprotonated forms of papaverine; and the cross-sections of the SERS bands of the protonated and deprotonated papaverine. This equation (eq 1) predicts that $Log_{10}\frac{S_{PH+}}{S_P}$ should track the pH with a slope of one if one treats $Log_{10}\frac{[\sigma_P]}{[\sigma_{PH+}]} - Log_{10}K_a$ as an adjustable additive number, whose value was found to be 4.9 (Figure 4) suggesting that $Log_{10}\frac{[\sigma_P]}{[\sigma_{PH+}]} = -1.1$.

Figure 4 shows that the ratio does indeed decrease with decreasing pH (and hence with increasing papaverine concentration), but less rapidly than predicted by the analysis, perhaps signaling the fact that more than two bands contribute to the SERS feature observed in the range 700–780 cm^{-1}. Nevertheless, the self-consistency of these results strongly supports the overall picture we present for the dynamics and equilibria of papaverine hydrochloride in aqueous solution.

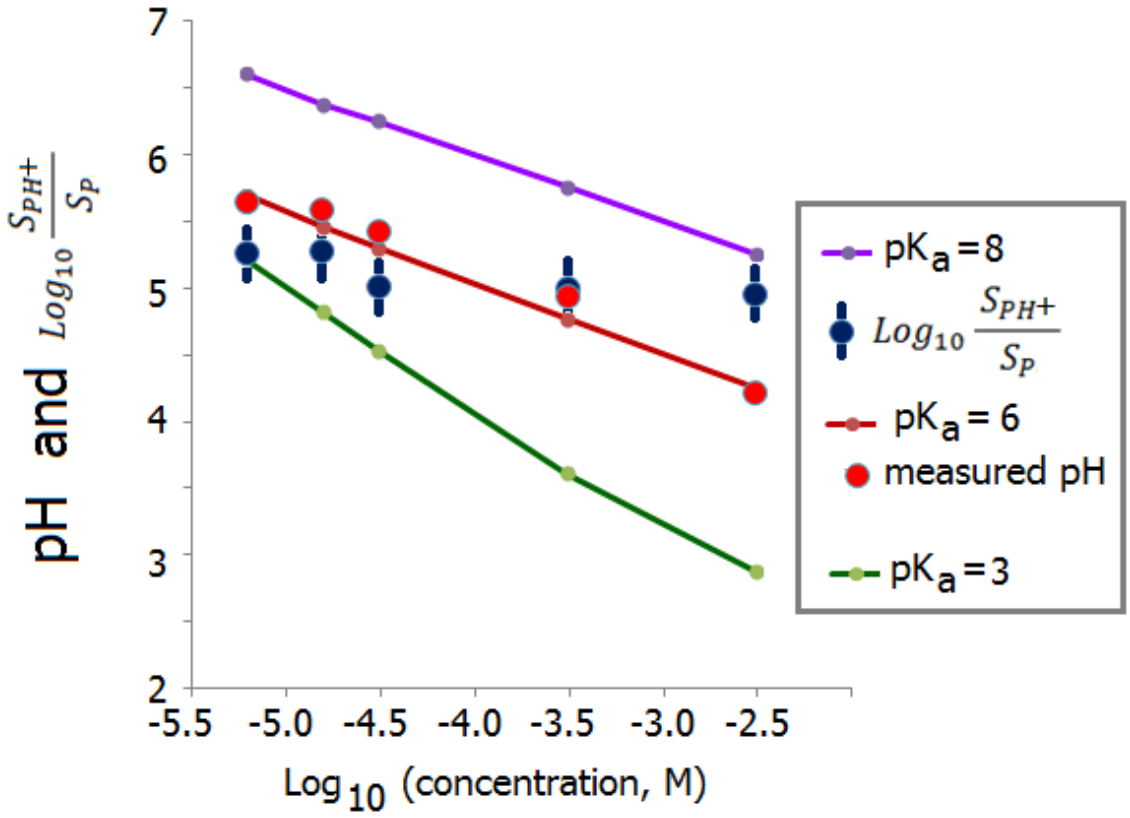

Figure 4. Measured (large red point) and calculated (lines) pH values of aqueous solution of papaverine hydrochloride as a function of concentration. Calculated values for various assumed values of pK_a are shown. The measured pH values agree well with $pK_a = 6$. Also shown are the Log_{10} ratios of the intensities of the SERS bands at 730 cm^{-1} to 769 cm^{-1} (large blue point) as a function of concentration. The ratio decreases with decreasing solution pH indicating that the 730 cm^{-1} band belong to the protonated form of papaverine in solution, while the 769 cm^{-1} band belongs to the deprotonated form.

3. DELECTROPHORESIS INDUCED SERS

3.1 DEP Theory and Approach

Migration of the nanoparticles in the device was modeled numerically using COMSOL Multiphysics V5.2 (www.comsol.com) to determine appropriate electrode geometries for effective nanoparticle trapping at low electrical potentials.

The electric field in the device was computed by solving Poisson's equation

$$\nabla^2\varphi = 0, \tag{2}$$

where φ is the electric potential.

Stokes' law was used for approximating the drag force on the nanoparticles,

$$F_{drag} = 6\pi r\eta \mathbf{v}, \tag{3}$$

where F_{drag} is the drag force acting on the particle, η is the dynamic viscosity of the fluid, r is the radius of the nanoparticle, and **v** is flow velocity relative to the nanoparticle.

Dielectrophoresis was modeled by the equation

$$<F_{DEP}> = 2\pi r^3 \epsilon_m \mathrm{Re}\left\{\frac{\epsilon_p^* - \epsilon_m^*}{\epsilon_p^* + 2\epsilon_m^*}\right\} \nabla |E|^2, \tag{4}$$

where $< F_{DEP} >$ is the time-averaged DEP force on the particle, *r* is the radius of the particle, ϵ_m is the real part of permittivity of the medium, E is the electric field, and ϵ_p^* and ϵ_m^* are the complex permittivities of the particle and the medium, respectively.

The migration velocity of the nanoparticles relative to bulk flow was calculated using force balance,

$$<F_{DEP}> + F_{drag} = 0. \tag{5}$$

The electrode geometry was lithographically patterned on 500 µm-thick fused silica wafer (University Wafers). 100 nm-thick gold electrodes were then formed by lift-off process, using a 15 nm-thick titanium adhesion layer. Since tin-based solders readily dissolve gold, a 100 nm-thick layer of nickel, covered by a 50 nm-thick gold layer was deposited on top of the gold contact pads. Upon contact with hot solder, the top gold layer dissolves allowing the exposed nickel layer to form a strong bond with the tin-based solder.

Microfluidic channels were made in PDMS (Sylgard 184, Dow Corning®) using soft-lithography using an SU-8 mold. The microfluidic channels were 100 µm wide and 20 µm deep. Inlet and outlet vias were produced in the PDMS using a biopsy punch. Corresponding inlet and outlet vias were drilled on a glass microscope slide. The electrode substrate, the PDMS, and the microscope slide were ozonated and the PDMS was sandwiched between the electrode substrate and microscope slide and aligned under a microscope using methanol as lubricant to allow electrode-to-microchannel fine alignment. Pipette tips were attached to the inlet and outlet vias using epoxy adhesive to form chip-to-world fluidic connections. Aluminum wires were soldered to contact pads on the electrode substrate to form the electrical connection between the chip and the electrical function generator.

To ensure device reusability, all wetted surfaces of the chip were passivated. A 5mM ethanolic solution of 11-Mercaptoundecyltetraethylene glycol (Sigma-Aldrich®) was incubated in the microfluidic channel to passivate the gold electrodes. Wetted PDMS and fused silica surfaces were fluorinated in a 1 mM solution of (Heptadecafluoro-1,1,2,2-tetrahydrodecyl) trichlorosilane (Gelest, Inc.) in FC-40 (Sigma-Aldrich®). A vacuum pump was used to establish flow of the reagent in the channel. The sub-atmospheric pressure was adjusted such that the

mean flow rate in the microchannel was approximately 5 µl/min. After 30 minutes of reagent flow, the microfluidic channels were flushed with ethanol followed by water, then baked at 50 °C overnight.

Saliva was collected from a healthy adult volunteer. Food and beverages were avoided for 30 minutes prior to sample collection. The volunteer did not use prescription or illicit drugs prior to sample collection. Undiluted saliva was spiked with (+)-methamphetamine hydrochloride (Sigma-Aldrich®) to a concentration of 500 nM. A separate sample was prepared using the same saliva batch and spiked with heroin hydrochloride (Sigma-Aldrich®) to a concentration of 50 µM to be used as the negative control. Saliva samples were then filtered using a 0.2 µm syringe filter (Millex®-FG) to remove cells and particles that could cause clogging of microfluidic channels. A 5 mM solution of (+)-methamphetamine was prepared in Milli-Q® DI-water to be used as the positive control. Citrate-capped 40 nm silver nanoparticles (Biopure, nanoComposix) were incubated in a 1 mM NaI solution in order to remove citrate from the surface of the nanoparticles to yield nanoparticles nearly free of background SERS spectra. The nanoparticles were then washed 3-times with Milli-Q® DI water and added to saliva samples at a concentration of 0.01 mg/ml.

Electrical connection was established between the function generator (Agilent Technologies, Inc., 33220A), AC voltage amplifier (FLE, F20A), and the chip. A 25 µl sample was loaded into the microfluidic device inlet reservoir and the flow was mobilized and adjusted to approximately 5 µl/min. The chip was loaded onto a LabRam Aramis Raman microscope (HORIBA, Ltd., Kyoto, JP), equipped with a 633-nm laser as the excitation source. The laser was focused on the DEP trap region using a 50X objective, exposing the sample to 0.78 mW of laser power. Microfluidic flow was subsequently stopped and an AC potential with a frequency of 2.5 MHz and an amplitude of 16 V_{pp} was applied to the electrode contact pads. SERS spectra were collected at 1-second integration intervals for a total of 150 seconds. After data acquisition, excess sample was removed from the inlet reservoir and replaced with DI-water. Flow was re-established at a higher rate of approximately 20 µl/min. An AC potential of 12 MHz at 80 V_{pp} was then applied to the electrodes. The combination of high flow rate and secondary electrokinetically-induced flow at the surface of the electrodes cleared the agglomerated nanoparticles in the trap region, thereby preparing the device for a new analysis run. The detection-clearance cycle was repeated three times with 500 nM methamphetamine-positive saliva samples, while 50 µM heroin-positive saliva samples were used as negative controls for the experiments.

Eigenvector PLS toolbox (Eigenvector Research, www.eigenvector.com) was utilized to construct a principal component analysis (PCA) model for the analysis of the spectra. SERS spectra from 5 mM methamphetamine reference stock and pure saliva were used to construct the calibration model. The baseline was subtracted from each of the acquired spectra using a weighted least-square filter, normalized by the area under the spectrum in the 500–1800 cm^{-1} range and finally mean-centered. Venetian-blinds with 10 splits were used for cross-validation. The portions of the SERS spectra in the 500–1800 cm^{-1} wavenumbers range were used for the analysis. Methamphetamine-positive saliva samples and heroin-positive saliva samples were then tested against the calibration model.

3.2 DEP Results

Uncapped silver nanoparticles are not thermodynamically stable and tend to aggregate shortly after synthesis. Various capping agents such as citrate, PVP, peptides, etc. are used to stabilize silver nanoparticles by electrostatic or electrosteric means. Capping agents are used to stabilize silver nanoparticles, thereby improving their shelf-life, but with the undesirable consequence of having the SERS spectrum of the capping agents interfere with that of the analyte, especially at low analyte concentrations. More importantly, the capping agent occupies surface adsorption sites that might otherwise be available to those analyte molecules unable to displace the capping agent. Methamphetamine is an analyte with low affinity for silver surfaces. As a result, we first removed as much of the citrate off the silver nanoparticles as possible by incubating the off-the-shelf citrate-coated 40-nm silver nanoparticles in a 1 mM sodium iodide solution. Others have previously used silver nanoparticles, modified with potassium iodide, for SERS studies of proteins and concluded that modification of silver nanoparticles with iodide removes surface impurities from particles while retaining stability and SERS activity. Here, the removal of the citrate from the surface of the nanoparticles was evidenced by the elimination of Raman bands associated with citrate. The Iodide-modified silver nanoparticles retained their SERS activity and remained stable for several days. Figure 5 shows SERS spectra collected from the silver nanoparticles before and after surface modification with sodium iodide, and the absorbance spectrum suggests minimal aggregation after surface modification of the silver nanoparticles with sodium iodide.

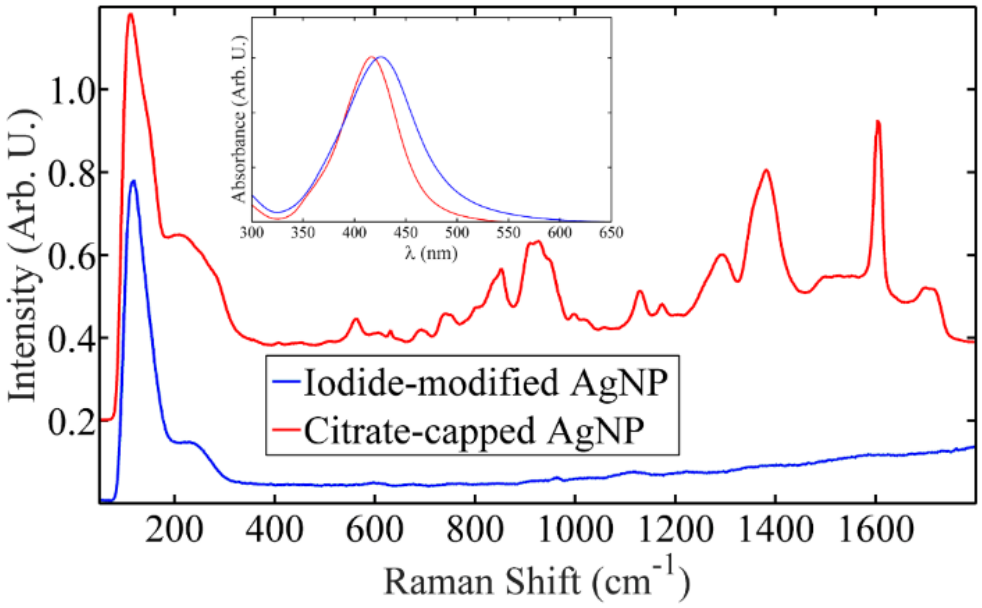

Figure 5. Comparison of background SERS spectra of off-the-shelf 40-nm citrate capped silver nanoparticles before (red) and after (blue) surface modification with sodium iodide. Surface modification with sodium iodide effectively removes citrate from the surface of the nanoparticles, resulting in elimination of background signal in the 400–1800 cm^{-1} wavenumber range. Nanoparticles retain their SERS activity and remain stable for days. Inset shows slight red-shift, without significant aggregation, after surface modification of nanoparticles with iodide consistent with the literature.[33]

Each device has four trap regions. A gap between the electrodes has a width of 7 μm (Figure 6). During device operation, the laser beam is focused by the Raman microscope on one of the four traps. It might then be moved to another trap after the spectra are acquired. DEP-induced agglomeration of the silver nanoparticles occurs primarily at the trap sites.

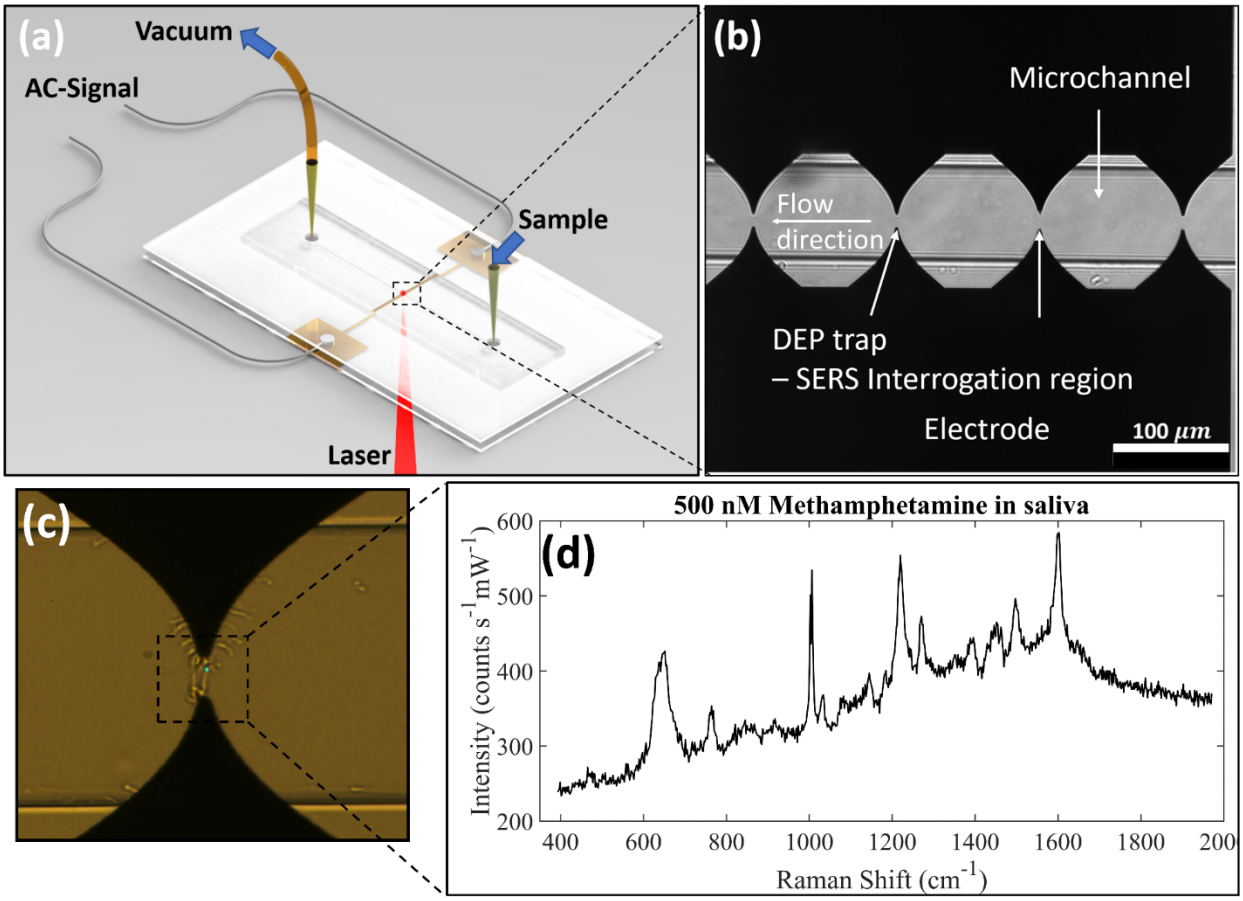

Figure 6. Depiction of the architecture of the DEP-SERS chip. (a) A PDMS microchannel is sandwiched between electrode substrate and glass cover. Yellow pipette tips form fluidic reservoirs/connections. Aluminum wire soldered to contact pads form the electrical connection between the chip and the AC signal generator. The chip is loaded onto the Raman microscope, upside down, to prevent laser light from transmitting through PDMS layer, effectively eliminating PDMS Raman interference. (b) Each device consists of four trap zones. Traps are aligned to the center of the channels for maximum flow shear during clearing of the microfluidic channels for subsequent detection cycles. (c) Close-up view of a single trap using agglomeration of nanoparticles. (d) Typical SERS spectra acquired using the DEP-SERS chip.

The direction of the DEP force is determined by the sign of the Clausius-Mossotti factor (depicted in brackets in eq 3), which accounts for permittivity contrast between the particle and medium. During the experiments, the AC potential frequency did not exceed 3 MHz. At these low frequencies, silver has very large dielectric constants, allowing the Clausius-Mossotti factor to be approximated by unity. This results in positive DEP, where nanoparticles migrate towards the electrode edges. Secondary electric field gradients, which are induced by the nanoparticles attached to electrode edges, further enhance the positive DEP effect

and result in additional agglomeration of nanoparticles at the trap site, a phenomenon known as pearl-chaining.[35]

In the current device, approximately two minutes are required to agglomerate the silver nanoparticles by DEP and acquire a SERS spectrum of nanomolar concentrations of methamphetamine in saliva with a signal-to-noise ratio of at least 10. A larger electric potential results in faster trapping and detection but can also cause water electrolysis, electrode damage, nanoparticle melting, and subsequent short-circuiting of the electrodes. Hence, the lowest workable electric potential was used. Appropriate design and dimensions for such electrodes were determined using numerical simulation. Figure 7 shows the cross-sectional view of the microfluidic channel at mid-plane of one of the trapping zones. Contours of constant $\mathbf{E}^2$ are shown as black lines. Red lines, showing the migration path of the nanoparticles towards the trap, are orthogonal to the contours of constant $\mathbf{E}^2$ as expected from eq 5.

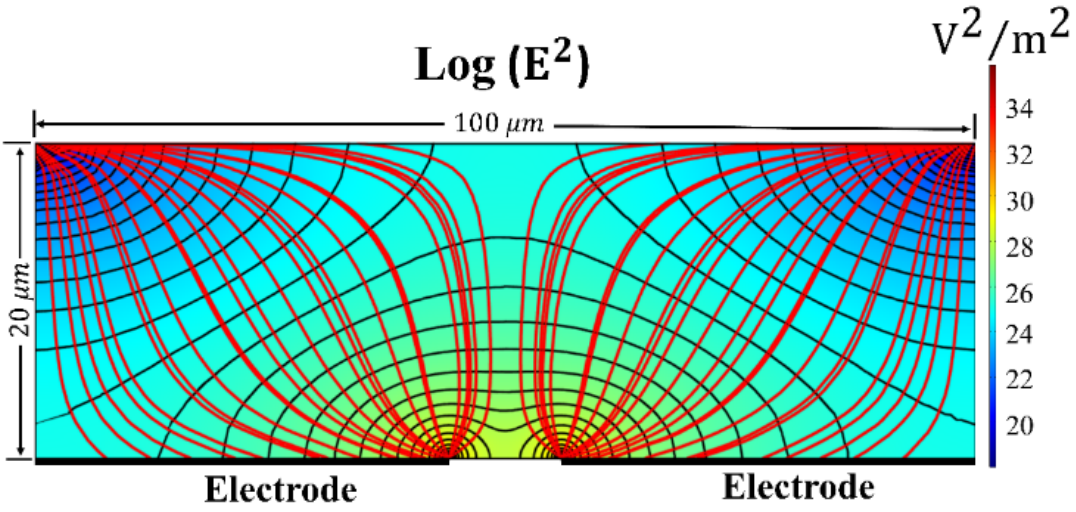

Figure 7. Numerical Simulation of silver nanopartical electromigration. Cross-sectional view of the microfluidic channel at mid-plane of one of the trap zones. Black lines correspond to contours of constant $|\mathbf{E}|^2$. Red lines show path lines of the nanoparticles towards the trap. Highly polarizable nanoparticles migrate from the regions of low electric field intensity to regions of high electric field intensity.

The flow is stopped shortly after the sample is loaded in the microfluidic device and remains stopped during signal acquisition. Migration of the nanoparticles is solely due to diffusion and electrokinetics during each acquisition cycle. Since the location of the DEP-aggregated SERS-active substrate is spatially determined by the design of the electrodes, the optimal spatial location for collection of SERS spectra is also determined by these design parameters. As a result, SERS spectra were successfully collected from trapping zones that were determined by computation without the need to first raster scan the device to find the maximal signal intensity.

Saliva samples were premixed with freshly prepared iodide-modified silver nanoparticles and loaded into the device. In a typical detection run, sample flow is established, the device is placed on the microscope platform of the Raman spectrometer, and the laser focused with a 50X objective lens onto one of the four trap regions. The fluid flow is stopped

and a 16 V_{pp}, 2.5 MHz AC-potential is applied to the electrodes. The SERS signal intensity increases with time, due to the agglomeration of the nanoparticles by DEP, reaching a maximum intensity after approximately 120 s. Additional nanoparticles are likely accumulated beyond this time but do not significantly contribute to the signal collected.

Although at higher concentrations the nanoparticles agglomerate faster and improve the time-response of the device, they tended to foul the microchannels after long detection runs. For this reason, the relatively low nanoparticle concentration of 0.01 mg/ml was used in all of the experiments.

Experiments were carried out with: (i) pure saliva, (ii) 5 mM methamphetamine in DI water as reference samples, (iii) 500 nM methamphetamine in saliva as test samples, and (iv) 50 µM heroin in saliva as negative controls. A methamphetamine cut-off limit of 500 nM is lower than concentrations routinely observed in oral fluids of impaired individuals. Figure 8 shows a comparison of time-averaged raw spectra for the aforementioned samples.

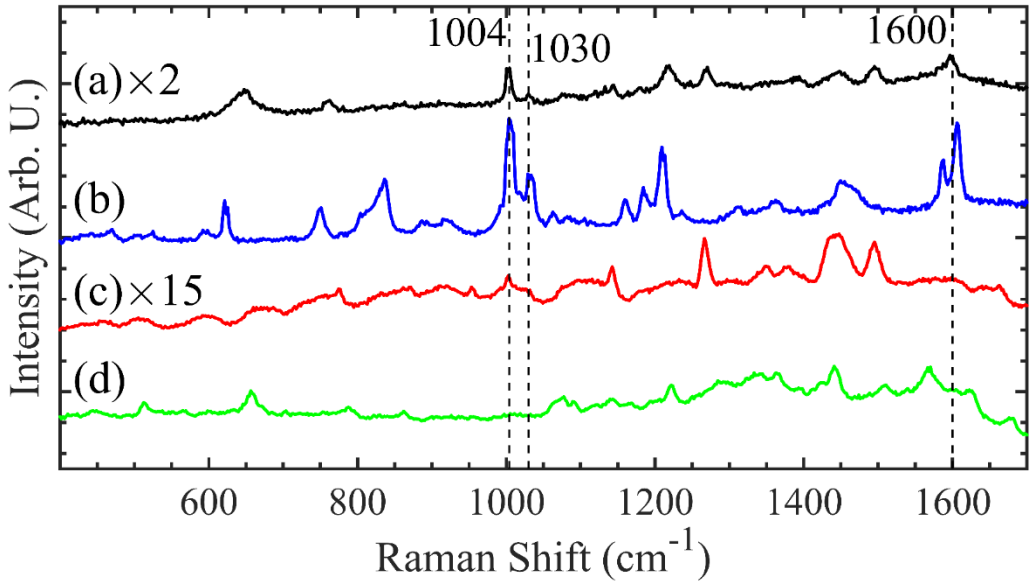

Figure 8. Raw spectra acquired using the DEP-SERS chip. Peaks at 1004 cm^{-1}, 1030 cm^{-1} and 1600 cm^{-1} discriminate methamphetamine-positive saliva samples from pure saliva samples. (a) 500 nM methamphetamine in saliva, averaged over 5 s. (b) Methamphetamine reference (5 mM in DI water), averaged over 5 s. (c) Saliva reference, averaged over 20 s. (d) 50 µM heroin in saliva, averaged over 10 s.

Saliva is a complex fluid with inter-individual and intra-individual variability in composition. The many SERS bands observed here likely originate from small protein molecules present in saliva.[36] The 1004 cm^{-1}, 1030 cm^{-1}, and 1600 cm^{-1} known methamphetamine Raman vibrational modes (phenyl ring modes),[37,38] effectively identify a methamphetamine-positive saliva sample from pure saliva, even without chemometric analysis.

Figure 9 summarizes the time-evolution of SERS spectra for the methamphetamine-positive saliva sample. Within a few seconds of application of AC potential, SERS spectral features corresponding to saliva and methamphetamine appear as the

nanoparticles agglomerate at the trap. Once the AC potential is applied, the signal intensity grows monotonically until it reaches a maximum intensity in approximately 120 seconds.

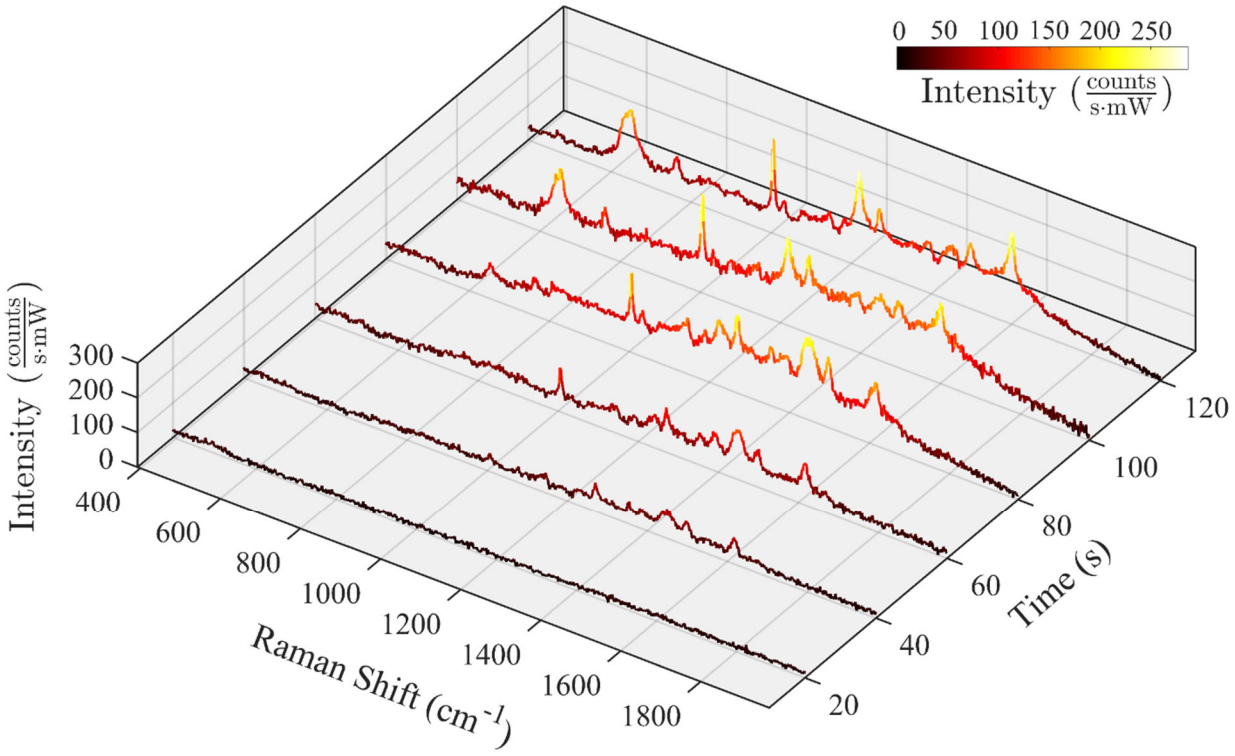

Figure 9. Evolution of spectra for 500 nM methamphetamine-positive saliva sample. Linear baseline correction is applied to the spectra. As nanoparticles agglomerate in the traps, the signal intensity increases until it plateaus at around 120 s.

A principal component analysis model with two principal components was found to capture 69.57 % of the overall variance of the spectra. The rest of the variance is attributed to noise and chemical intra-variability of the highly complex saliva matrix. A comparison between principal component loadings and SERS spectra of methamphetamine and saliva reveals that PC1, accounting for 66.80 % of the overall variance of the data, is mainly comprised of spectral features that separate saliva from methamphetamine. PC2, which captures 2.77 % of overall variance, describes some of the intra-sample variations of the raw saliva. After construction and cross-validation of the PCA calibration model, heroin-positive and methamphetamine-positive saliva samples were tested against the model. Figure 10 summarizes the results of the principal component analysis of the test datasets together with the calibration datasets. As shown, the plot of PC1 versus PC2 clearly discriminates methamphetamine-positive samples from pure saliva wherein the associated ellipses correspond to 95 % confidence intervals. Heroin-positive saliva samples, which play the role of negative-control for the PCA model, are also separated well from the other samples. It is worth noting that since the model is mean-centered, a sample with a PC1 score of zero would have equal contributions from spectral features of methamphetamine and saliva; whereas a positive PC1 score indicates a greater methamphetamine contribution over that of saliva.

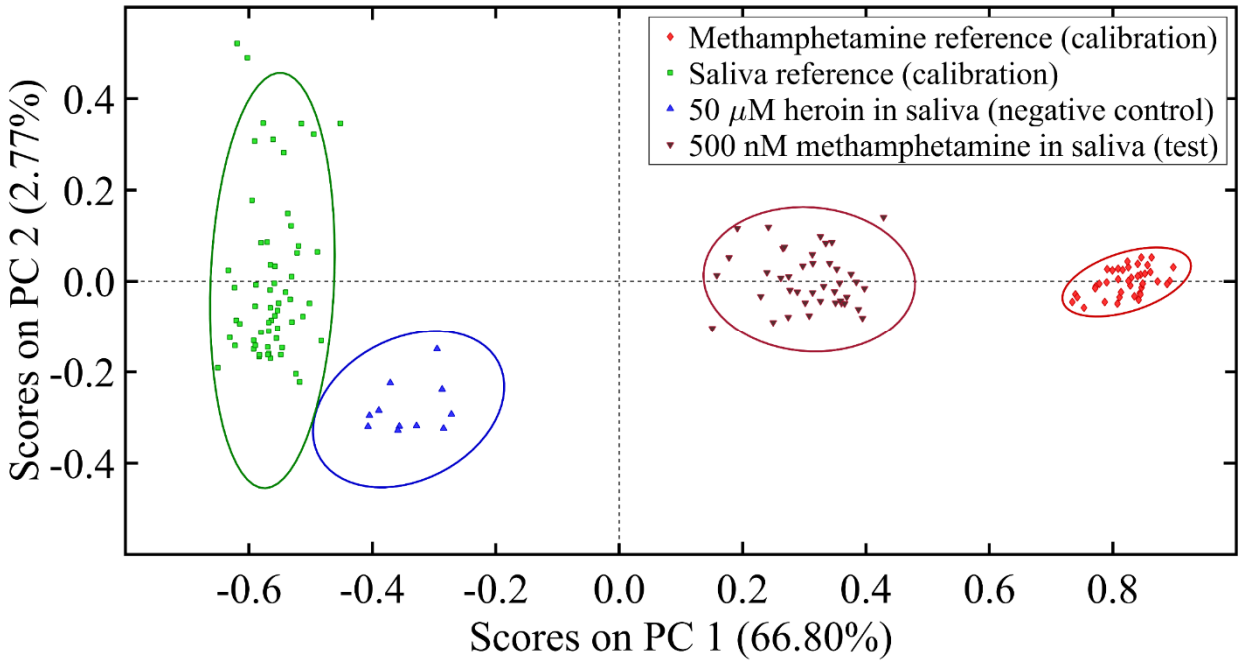

Figure 10. PCA scores plot for the calibration and test datasets. Calibration model was constructed using pure saliva and methamphetamine reference datasets. Methamphetamine-positive saliva samples and heroin-positive saliva samples were tested against the model. A 2-PC model provides good separation of the samples. The ellipses correspond to 95 % confidence intervals.

4. QUANTITATIVE SERS ANALYSIS

4.1 Experimental Approach

The microfluidic device was designed in a flow-merging arrangement that unites three separate inlet laminar flows of AgNP, LiCl (an aggregation agent), and analyte solutions into a single channel with a single outlet. The laminar flow is critical to the device's operation so that cross-stream transport occurs only through diffusion. The flow merging microfluidic device was fabricated using standard soft-lithography techniques. Briefly, uncured liquid polydimethylsiloxane (PDMS, Dow Corning® SYLGARD™ 184) was mixed and poured onto a silicon wafer with SU-8 epoxy photoresist hills with the desired features patterned. The PDMS was cured in an oven at 80 °C for 1.5 hours. The PDMS layer was then removed and cut to fit a regular 25-mm x 75-mm glass slide in which fluidic vias had been drilled. The microfluidic channels were 20 µm deep by 50 µm wide. PDMS and glass was then exposed to ozone for 10 minutes and pressed into contact creating a permanent seal.

The device was loaded with 20 µL of 0.02 mg mL^{-1} 40 nm AgNP (NanoXact, nanoComposix) and 20 µL of 0.2 M LiCl (Sigma-Aldrich®, Merck KGaA) in the respective flanking inlets. The center inlet was loaded with various concentrations of methamphetamine, papaverine, or cocaine (Sigma-Aldrich®, Merck KGaA). The channels were then primed up to

the merging junction with positive pressure from a syringe, then operated by applying vacuum to the outlet, and allowed to flow for at least 2 minutes before raster scanning a 50-µm x 100-µm portion of the channel in the Raman microscope (HORIBA, Ltd., Kyoto, JP) to locate a strong SERS signal. The interrogation began 100 µm downstream of the junction. A 50X objective lens was used, together with a 633 nm laser at a power of 83 µW with a two-second exposure at each interrogation point.

The collected data were analyzed with the PLS toolbox (Eigenvector Research, Inc.) the CLS module. Model spectra (loadings) were collected for each analyte as well as citrate. The loadings spectra were collected using freshly prepared BH_4^- capped AgNPs and high concentration analyte solutions (> 3 mM) in a device. Citrate loading spectra were collected using deionized Milli-Q® water (18.2 MΩ) as the analyte in a working device. The preprocessed loadings in the CLS model are shown in Figure 11.

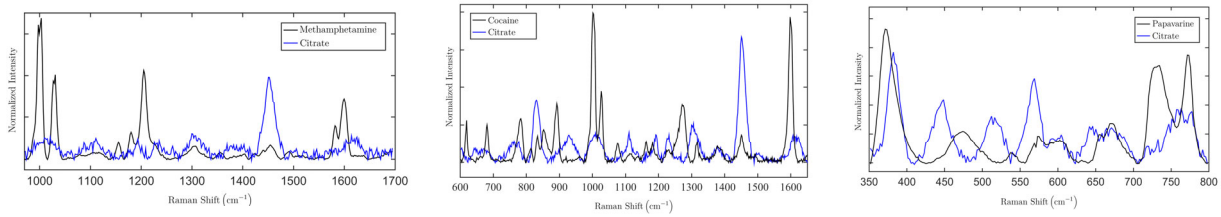

Figure 11. CLS model spectra of methamphetamine (left), cocaine (middle), and papaverine (right), in which citrate spectra are also included. Preprocessing consisted of baselining and normalization by area under the curve of spectra. Respective molecular structures of the analytes are also shown.

Acquired raw spectra from serially-diluted analyte samples were processed as follows. Spectra with intense 229 cm^{-1} bands, characteristic of AgNPs aggregates, were included in the analysis. The remaining spectra, which originate from regions in the microfluidic channel with no aggregates, were not analyzed. Spectra were then baselined using an automatic Whittaker filter ($\lambda = 100$ and $P = 0.001$), followed by normalization by the area under the spectrum of each, in the wavenumber ranges, shown in Figure 11. Preprocessed spectra were then fitted using the CLS model and relative contributions of citrate and the analyte to the spectra were calculated.

4.2 Chemometric Analysis

The spectral loadings that were used for CLS model generation resembled spectra typically reported in the literature. The spectral regions that were selected for analysis (depicted in Figure 2) were chosen to improve the discrimination between the citrate background, while capturing the dominant Raman modes of the analytes. For each analyte (methamphetamine, cocaine, and papaverine) a series of spectra at various concentrations were collected. Concentrations of analytes were decreased by dilution until no significant score of the analyte was returned by the CLS analysis. The significance of the score is assessed by testing a negative control sample with no analyte against the CLS model whereby a cut-off limit with 95 % confidence limit was established. The limits of detection determined in this manner for methamphetamine, papaverine, and cocaine were 100 nM, 500 nM, and 100 nM, respectively. The range of concentrations of methamphetamine and cocaine detected covered the range of

forensic and toxicology values normally reported. The concentrations of papaverine observed were within concentration ranges pertinent in forensic contexts. The scores for each concentration of analyte was calculated from a minimum of five spectra. The calculated scores versus concentration are reported in Figure 12. A similar trend is observed for each analyte, with the citrate score decreasing as the analyte concentration increases, implying that the analyte displaces citrate off the AgNPs and into solution. The effect of the Cl^- ions from LiCl was considered to be constant as new AgNP and analyte solution were constantly being provided, creating steady-state conditions. The quantity of citrate displaced from the surface of the AgNP was (not unexpectedly) found to be a function of: (i) the concentration of the analyte, (ii) the time of exposure of analyte to AgNP, and (iii) the competitive affinity of the analyte versus citrate for silver surfaces. Qualitatively, it is clear that papaverine has a lower affinity for the AgNP than either cocaine or papaverine. Its lowest detectable concentration was 500 nM, while each of the two other analytes had approximately an order of magnitude lower limits of detection.

We also show that papaverine has a lower propensity to displace citrate from the Ag surface than methamphetamine and cocaine, which is also consistent with the "crossover" concentration values shown in Figure 12.

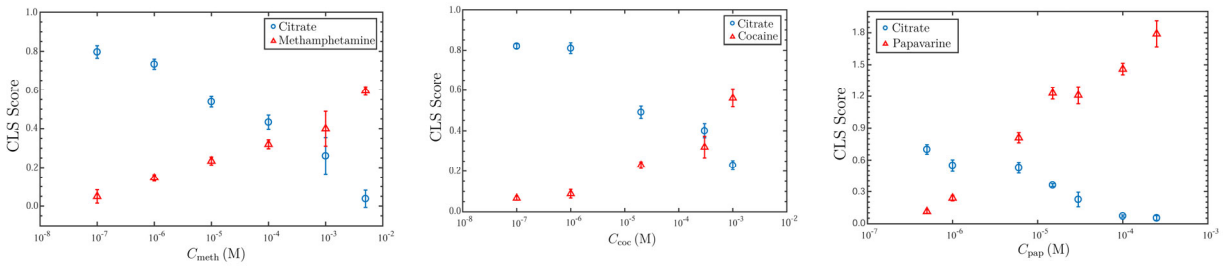

Figure 12. Least squares analysis scores for the SERS spectra of methamphetamine (left), cocaine (middle), papaverine (right), and citrate as a function of concentration. The data is plotted as a function of the natural log of concentration. 95 % confidence intervals are shown for each data point. Note: the crossover concentration for papaverine is much lower than for the other two analytes.

4.3 Adsorption Kinetics

In order to acquire a better understanding of our observations and to facilitate the quantitative determination of the unknown concentration of a collected sample, we develop a model that yields a function relating the measured SERS intensities of the analyte and citrate to the concentration of the analyte in solution.

Denoting the analyte as species 1 and citrate as species 2, the rate equations describing these processes are given as

$$\frac{dN_1}{dt} = k_1 c_1 (S - N_1 - N_2) - k_{-1} N_1, \tag{6}$$

for analyte, and

$$\frac{dN_2}{dt} = k_2 c_2 (S - N_1 - N_2) - k_{-2} N_2, \quad (7)$$

for citrate—in which N_1, k_1, c_1, k_{-1}, and S are, respectively, the number of analyte molecules on the silver surface; the adsorption rate constant of the analyte; the concentration of the analyte in solution; the desorption rate constant of the analyte; and the total number of adsorption sites on the surface. Analogous parameters for citrate are subscripted 2.

At steady state,

$$\frac{dN_1}{dt} = \frac{dN_2}{dt} = 0. \quad (8)$$

Substituting Equations 6 and 7 into 8 and simplifying yields

$$\frac{N_1 k_{-1}}{c_1 k_1} = \frac{N_2 k_{-2}}{k_2 c_2}. \quad (9)$$

Assuming the silver surface is initially saturated with citrate—and the citrate concentration in solution is zero—the steady-state concentration of citrate in solution (c_2) depends solely on the quantity of analyte (N_1) that adsorbs on the surface.

We propose the relationship

$$c_2 = b N_1^n, \quad (10)$$

in which b is a proportionality constant and n is an analyte-specific parameter that relates the number of citrate molecules displaced per analyte molecule adsorbing on the silver surface. This depends on multiple factors, chief among them the relative size of the area occupied by an analyte molecule as compared to a citrate molecule. A large analyte molecule could displace several citrate moieties and therefore be characterized by a larger n value.

Substituting eq 9 into eq 10 yields

$$\frac{N_1^{1+n}}{N_2} = \beta c_1, \quad (11)$$

where, $\beta = \frac{k_1}{k_{-1}} \frac{k_{-2}}{k_2 b}$.

Assuming the SERS signal is proportional to the number of molecules illuminated and therefore proportional to the CLS scores, one obtains the equation

$$\frac{S_1^{n+1}}{S_2} = \frac{\sigma_1^{n+1}}{\sigma_2} \beta c_1, \quad (12)$$

in which S_1 and S_2 are the SERS scores proportional to the SERS intensities of analyte and citrate, respectively, and σ_1 and σ_2 are parameters proportional to the Raman cross sections of the analyte and citrate, respectively. Because the range of concentrations (c_1) spans several orders of magnitude, we will fit our data in terms of logarithms of concentration; otherwise, the low concentration results will have no impact on the parameters retrieved.

Taking the logarithm of both sides of eq 12 produces a linear plot in $\log_{10}(c_1)$,

$$\log_{10}\left(\frac{S_1^{n+1}}{S_2}\right) = \log_{10}(c_1) + B, \tag{13}$$

where $B = \log_{10}\left(\frac{\sigma_1^{n+1}}{\sigma_2}\beta\right)$.

The scores of citrate, scores of the analytes, and concentration of analyte were fit using eq 1, optimizing n and B. The exponent values, n, returned by the fit for methamphetamine, papaverine, and cocaine were 2.6063, 5.3179, and 2.3867, respectively. The calculated data as well as the loadings for each analyte are presented in Figure 13. Note that the exponents on the Raman scores for methamphetamine and cocaine is more than twice that for papaverine, in agreement with the magnitudes of the Raman cross-sections for those species relative to that of citrate shown in Figure 11.

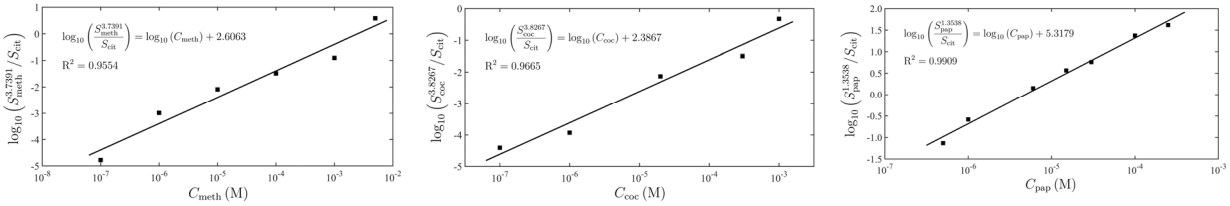

Figure 13. Calculated Raman score ratios as function of natural log of the analyte concentration for methamphetamine (left), cocaine (middle), and papaverine (right). The best fit line for each analyte is shown together with its function and R^2 value.

5. SERS SUBSTRATES FOR FORENSICS DETECTION

Silver and gold have dominated the SERS literature since the inception of the field, on account of their favorable and high quality plasmonic properties in the visible region of the spectrum and their high chemical stability. Indeed, the phenomenon was originally observed on roughened silver surfaces that are still commonly used as SERS platforms in biological applications, for detecting low concentration analytes, and in other sensing applications. Not unexpectedly, a great deal of interest has been focused on understanding both theoretically and experimentally what structural characteristics and materials properties lead to a highly effective SERS substrate for analytical applications.

Strategies for improving SERS performance have largely centered on optimizing the architecture of SERS substrates—for example, by developing strategies for reproducibly

aggregating nanoparticles, or producing such electromagnetically coupled nanostructures as nano-gratings, piezoelectrically driving a nanotip towards a metal surface as in tip-enhanced Raman spectroscopy (TERS), and synthesizing core-shell nanoparticles, in which the plasmon of a nanocavity couples to the plasmon of a nanosphere. It has been known from the earliest days of SERS that most metals can sustain plasmons, among which only the alkali metals rival the coinage metals in their plasmonic capabilities. Although excellent SERS results were reported with alkali metals under ultra-high vacuum conditions, their lack of stability in air and in water make the alkalis impractical for most applications. The plasmonics properties of other high conductance metals have been explored theoretically including Cu, Pt, Pd, and early SERS results using Al, Pt and In have been reported. The plasmonic resonance quality (i.e., the "sharpness" of the resonance) has been discussed by several workers. It is easy to show that the breadth of the plasmon resonance of a sphere, whose radius is much smaller than the wavelength, increases with increasing electron scattering rate (which is inversely proportional to electrical conductivity) and with increased interband contribution to the material's dielectric constant in the frequency range of the plasmon. (These two properties account for the good plasmonic performance of silver). Also well-known is the fact that the plasmon resonance frequency can be significantly tuned by altering the nanogeometry of the plasmonic entit7—for example, one (or more) of the three degenerate plasmonic modes of a Pd nanosphere (in air) whose resonance occurs at ~230 nm can be shifted to cover the entire visible and near-infrared (IR) spectrum by either elongating the sphere to a prolate spheroid or flattening it to an oblate spheroid.

Previously, we reported a nano-grating architecture that produces both highly enhancing and highly uniform SERS signals over wafer-scale areas. The grating consisted of two-dimensionally periodic silicon posts coated with silicon dioxide and metal thin films, creating a highly regular square array of core-shell nanoparticles whose average enhancements exceeded most nanoparticle aggregates by two or more orders of magnitude. The key to the strong performance of this architecture, which was reported using a gold metallic layer, is the synergy of local near-field resonances resulting from interactions between neighboring grating elements and long-range grating resonances. The nature of the grating contribution has been capably discussed in the literature—an important point being that grating resonances are, to first order, a function of the geometrical parameters of the grating, independent of the material. Here, we apply such architectural principles to a variety of metals to show that the grating-enabled plasmonic resonances allow a wide range of metals to function effectively as SERS active systems.

Expanding the pool of SERS-capable metals beyond silver and gold has important implications. For example, Aluminum is Earth-abundant and therefore inexpensive; and nickel, copper, platinum, palladium, and many other transition metals make possible the study of important surface chemical and catalytic processes, using SERS. Although few such attempts have appeared—none discussing the ubiquity of plasmonic materials systematically as we do here—such goals are not altogether new. For example, Michael Weaver pioneered studies in the 1980s using palladium-coated gold electrodes, and others followed, motivated by the desire to use SERS for studying chemistries for which gold is not suitable.

Here we demonstrate that by using a prescriptive top-down nanofabrication method, a silicon/silica nanograting can serve as a common substrate on top of which essentially

any metal can be deposited to create a highly functional SERS substrate. We illustrate this using five metals: gold, silver, copper, aluminum, and nickel. The first two—traditional SERS materials—are the benchmarks against which the performance of the others are compared. Copper was chosen to complete the set of coinage metals, and to illustrate the negative effects on enhancement of interband transitions occurring in the vicinity of the plasmon resonance. Aluminum is earth abundant and a good conductor whose dielectric function in the visible region of the spectrum is almost devoid of interband contributions. Nickel is not a particularly good conductor and has strong interband transitions in the visible; but it is a metal with rich surface chemistry.

As previously reported, the architecture consists of a 330 nm pitch 2D grating patterned using laser interference lithography followed by reactive ion etching. Plasma-enhanced chemical vapor deposition is used to deposit silica so as to reduce the gap between neighboring grating elements, followed by metal deposition using either electron-beam or thermal evaporation, creating a two-dimensional grating of closely-spaced core-shell nanostructures. For the systems studied here, 200 nm of silica were deposited followed by 104 nm total thickness of metal. Electron-beam evaporated metals are deposited to a thickness of 100 nm preceded by deposition of a 4 nm titanium adhesive layer. For metals deposited by thermal evaporation, the Ti adhesive layer is omitted, so the metal is deposited to a thickness of 104 nm. Scanning electron microscopy reveals that the grating architecture is effectively maintained for all choices of metal (Figure 14). While minor variations in surface roughness occur, most notably for nickel, the high uniformity of the two-dimensional grating arrangement of core-shell elements is apparent for all five metals over large areas as shown in Figure 14f for silver over several square microns.

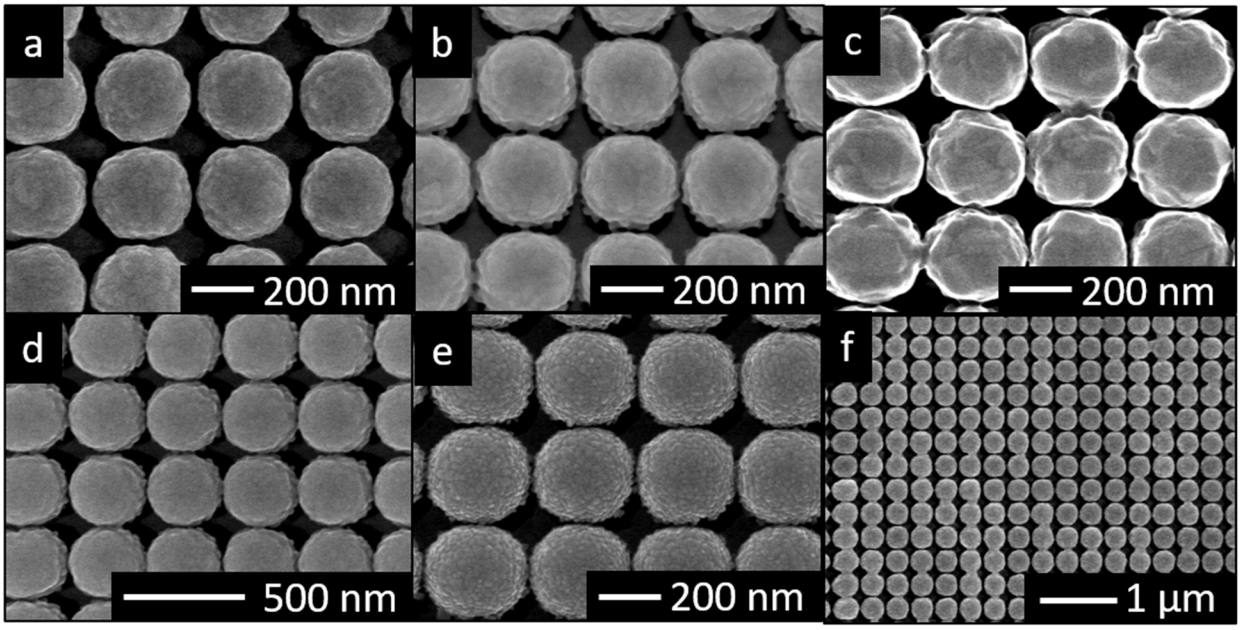

Figure 14. Scanning electron micrographs for SERS substrates fabricated with (a) silver, (b) gold, (c) aluminum, (d) copper, and (e) nickel show that repeatability of the topography previously shown with just gold. The uniformity is retained across several square microns as seen in (f).

The resonances of these systems were determined using reflectance spectroscopy at normal incidence, from which the absorbance was calculated by noting that the transmittance is zero. As seen in Figure 15, the absorbance spectra for all of the substrates is composed of several absorbance features among which two can be assigned directly. The first, and most prominent feature occurs at approximately 600 nm and corresponds to a radiative, first-order grating resonance. The fact that this resonance overlaps the 633 nm laser used in SERS experiment is no accident; the pitch of the grating was selected explicitly to achieve this overlap,[12] thereby ensuring strong SERS enhancement. While the maximum of this resonance does not exactly overlap with 633 nm for all of metals used, the pitch of the grating could be further fine-tuned to do so for each metal if that level of precision is desired. The other prominent feature occurs beyond 800 nm and is representative of near-field effects. A simple effective medium calculation for the corresponding silica@metal core-shell particles suggests that these absorption peaks are resonances due to the near-field interactions between neighboring elements.

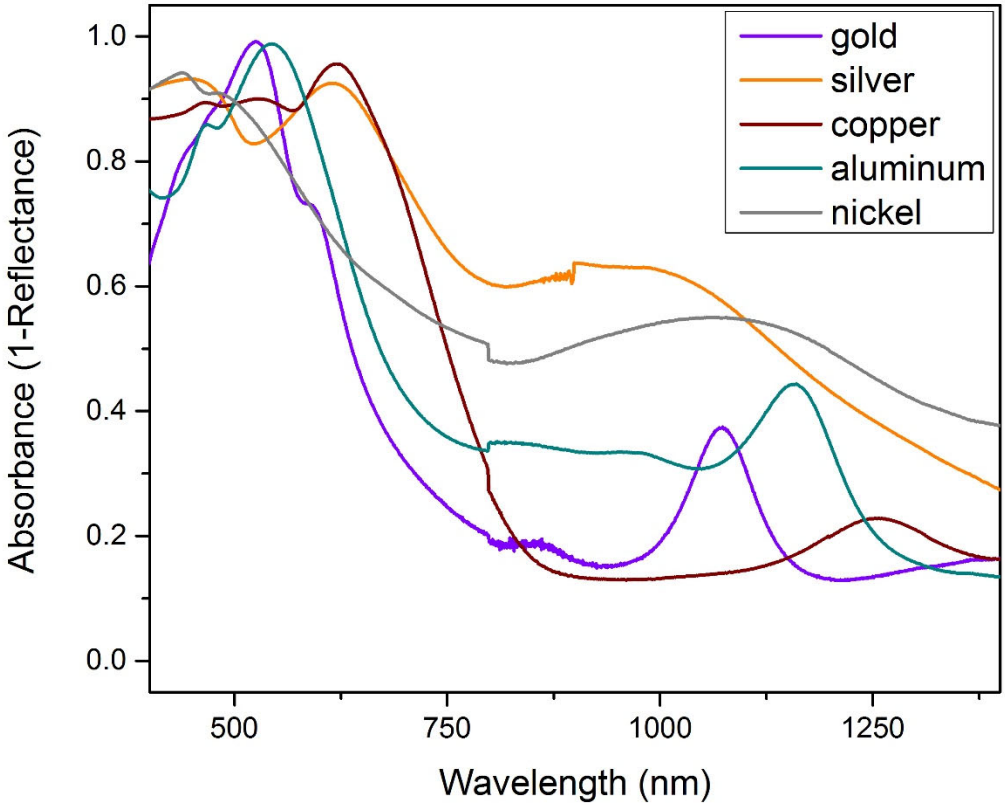

Figure 15. Absorbance (1- Reflectance) versus wavelength as measured at normal incidence by a UV-visible/near-IR spectrophotometer for all five choices of metal. For substrates of each metal, two major features can be observed—a radiative first order grating resonance near 600 nm and a core-shell resonance that occurs beyond 800 nm.

SERS performance was demonstrated with thionine adsorbed to full monolayer coverage. Un-adsorbed thionine was washed away and SERS spectra collected in backscattering mode using 7.6 microwatt incident power from a 633 nm laser and 0.25–2.5-second exposures. All reported values for SERS intensity are converted to counts per milliwatt per second for direct comparison.

Silver and aluminum substrates were pretreated to remove air-formed oxides. Silver and aluminum substrates were submerged in millimolar hydrochloric acid, and millimolar sodium hydroxide, respectively. Silver, not unexpectedly, gives the highest SERS intensity, outperforming the previously reported gold substrates by a factor of 4–5. Figure 16 shows thionine spectra as observed from each metal substrate. The measured SERS intensities (highest to lowest) were in the following order: silver, gold, copper, aluminum, nickel.

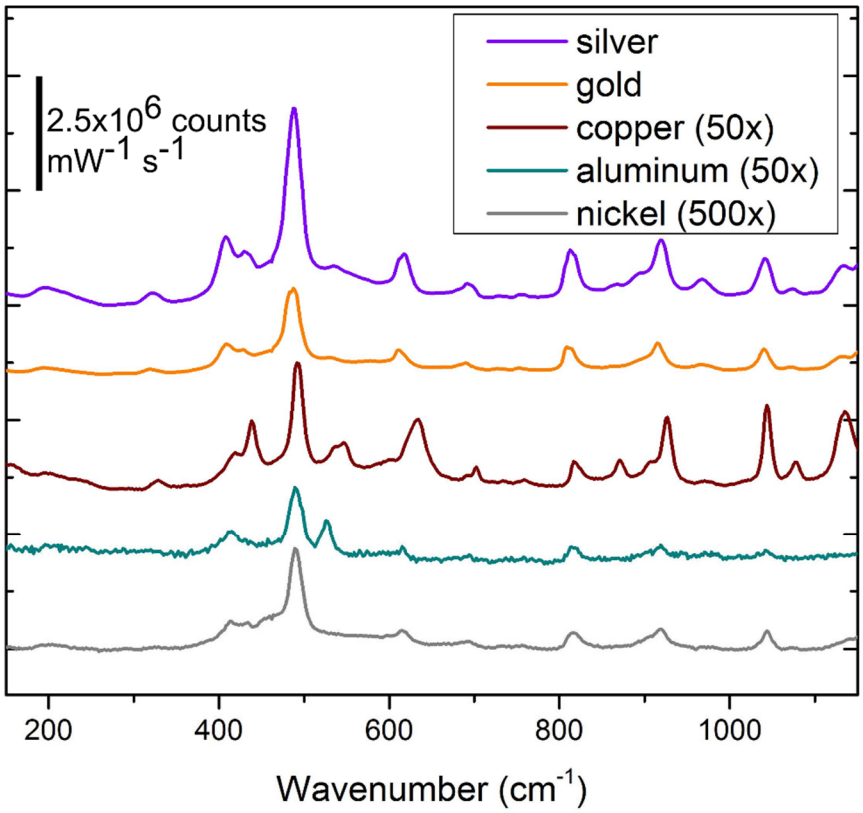

Figure 16. A comparison of SERS intensity observed for thionine adsorbed onto substrates of each of the five metals. Full monolayer coverage is assumed. Metals are presented in order of observed SERS intensity. Silver gives the most intense SERS as is expected based on theoretical calculations and experimental results from the literature. Here, silver gives 4.3×10^6 counts per milliwatt per second and is followed by gold.

To better account for the near field contributions to the SERS enhancements (which should largely account for most of the measured enhancement variations among the five metals), numerical simulations were carried out using a simple system of two closely-spaced silica@metal core-shell particles (Figure 17 inset) The experimental and simulated intensities

presented in Figure 17 are, respectively, scaled to the experimental and simulated SERS intensities measured and calculated for the silver substrate. The agreement between the observed relative SERS enhancement magnitudes and metal to metal trends and the calculated values is quite good, suggesting that the major source of enhancement originates from the grating effect, which contributes approximately the same level of enhancement for each of the metals. This implies that it is the near field contribution that accounts for the major source of variation in the SERS enhancement among the five metals, reported in Figure 17. Previously, we showed that a gold-based grating substrate with an architecture similar to what we describe here and with optimized structural parameters produced a SERS enhancement of 6×10^6 for adsorbed thionine when compared to the same number of molecules adsorbed on bulk gold.

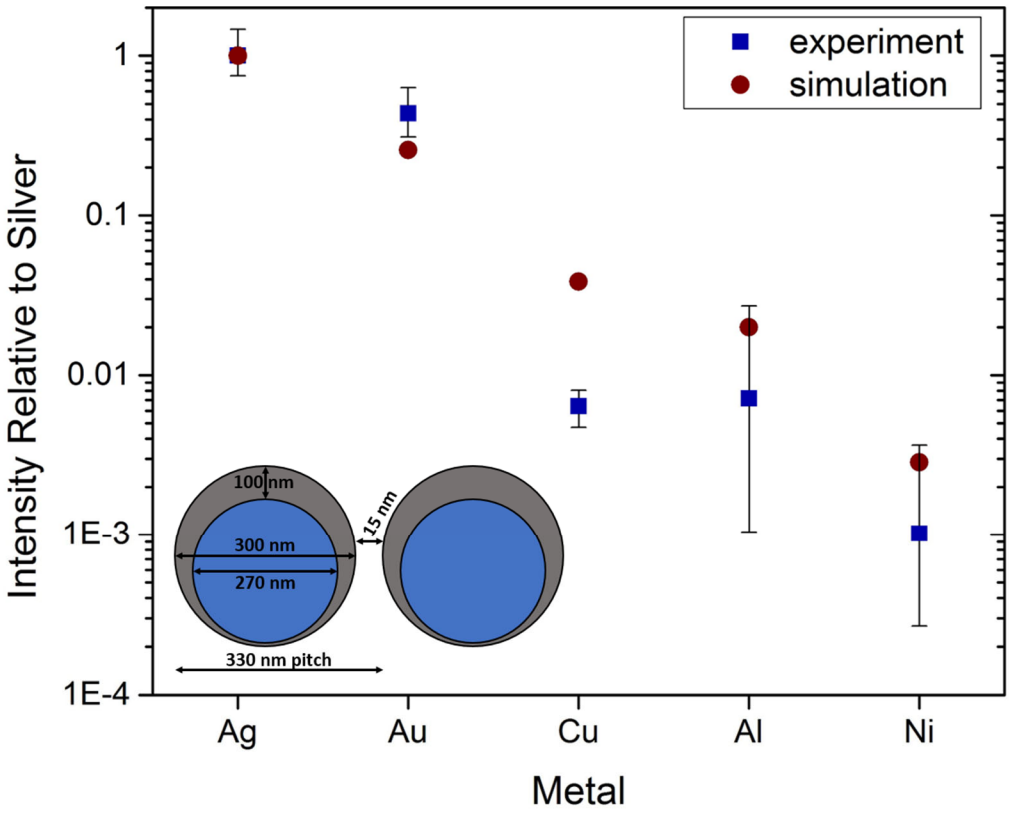

Figure 17. Relative experimental SERS intensities are compared to relative simulated intensities. All values are scaled to those of silver. Accordingly, the value of the relative enhancement for silver, the most enhancing metal of the five is unity and that for all other metals is less than unity. The simulated results show that the expected intensities span three orders of magnitude, which can be traced back to the dielectric functions of each metal. The experimental data trends with the simulated results, and while this means that the measured SERS intensities span three orders of magnitude, even the least enhancing metal, nickel, gives intensities on the order of 10^4 counts per milliwatt per second.

6. PUBLICATIONS

This section shows the publications that relate to this project.

6.1 2018 Publications

Salemmilani, R.; Piorek, B.D.; Mirsafavi, R.Y.; Fountain, A.W.; Moskovits, M.; Meinhart, C.D., Dielectrophoretic Nanoparticle Aggregation for On-Demand Surface Enhanced Raman Spectroscopy Analysis. *Anal. Chem.* **2018,** *90* (13), pp 7930–7936.

Salemmilani, R.; Mirsafavi, R.; Fountain, A.W.; Moskovits, M.; Meinhart, C., Quantitative Surface Enhanced Raman Spectroscopy Chemical Analysis using Citrate as an in-situ Calibrant. Analyst. Submitted 10 NOV 2018.

6.2 2017 Publications

Mirsafavi, R.Y.; Lai, K.; Kline, N.D.; Fountain, A.W.; Meinhart, C.D.; Moskovits, M., Detection of Papaverine for the Possible Identification of Illicit Opium Cultivation. *Anal. Chem.* **2017,** *89* (3), pp 1684–1688

Kanipe, K.N.; Chidester, P.P.F.; Stucky, G.D.; Meinhart, C.D.; Moskovits, M., Properly Structured, Any Metal Can Produce Intense Surface Enhanced Raman Spectra. *J. Phys. Chem. C.* **2017,** *121* (26), pp 14269–14273.

6.3 2016 Publications

Kline, N.D.; Tripathi, A.; Mirsafavi, R.; Pardoe, I.; Moskovits, M.; Meinhart, C.; Guicheteau, J.A.; Christesen, S.D.; Fountain, A.W., Optimization of Surface-Enhanced Raman Spectroscopy Conditions for Implementation into a Microfluidic Device for Drug Detection. *Anal. Chem.* **2016,** *88* (21), pp 10513–10522.

Kim, N.H.; Meinhart, C.D.; Moskovits, M., Plasmon-Mediated Reduction of Aqueous Platinum Ions: The Competing Roles of Field Enhancement and Hot Charge Carriers. *J. Phys. Chem. C.* **2016,** *120* (12), pp 6750–6755.

Kanipe, K.N.; Chidester, P.P.F.; Stucky, G.D.; Moskovits, M., Large Format Surface-Enhanced Raman Spectroscopy Substrate Optimized for Enhancement and Uniformity. *ACS Nano.* **2016,** *10* (8), pp 7566–7571.

6.4 2015 Publications

Hoonejani, M.R.; Pallaoro, A.; Braun, G.B.; Moskovits, M.; Meinhart, C.D., Quantitative multiplexed simulated-cell identification by SERS in microfluidic devices. *Nanoscale.* **2015,** *7* (40), pp 16834–16840.

Andreou, C.; Mirsafavi, R.; Moskovits, M.; Meinhart, C.D., Detection of low concentrations of ampicillin in milk. *Analyst.* **2015,** *140* (15), pp 5003–5005.

Pallaoro, A.; Hoonejani, M.R.; Braun, G.B.; Meinhart, C.D.; Moskovits, M., Rapid Identification by Surface-Enhanced Raman Spectroscopy of Cancer Cells at Low Concentrations Flowing in a Microfluidic Channel. *ACS Nano.* **2015,** *9* (4), pp 4328–4336.

Tripathi, A.; Emmons, E.D.; Fountain, A.W.; Guicheteau, J.A.; Moskovits, M.; Christesen, S.D., Critical Role of Adsorption Equilibria on the Determination of Surface-Enhanced Raman Enhancement. *ACS Nano.* **2015,** *9* (1), pp 584–593.

LITERATURE CITED

1. Merlin, M.D., Archaeological Evidence for the Tradition of Psychoactive Plant Use in the Old World. *Econ. Bot.* **2003,** *57* (3), pp 295–323.

2. Degenhardt, L.; Charlson, F.; Mathers, B.; Hall, W.D.; Flaxman, A.D.; Johns, N.; Vos, T., The global epidemiology and burden of opioid dependence: results from the global burden of disease 2010 study. *Addiction.* **2014,** *109* (8), pp 1320–1333.

3. Steinitz, M.S., Insurgents, Terrorists and the Drug Trade. *The Washington Quarterly.* **2009,** *8* (4), pp 141–153.

4. National Institute on Drug Abuse (NIDA) https://www.drugabuse.gov (accessed Apr 14, 2017).

5. National Institute of Standards and Technology (NIST), https://www.nist.gov (accessed Apr 14, 2017).

6. Moskovits, M., Persistent misconceptions regarding SERS. *Phys. Chem. Chem. Phys.* **2013,** *15* (15), pp 5301–5311.

7. Wustholz, K.L.; Henry, A.I.; McMahon, J.M.; Freeman, R.G.; Valley, N.; Piotti, M.E.; Natan, M.J.; Schatz, G.C.; Van Duyne, R.P., Structure-activity relationships in gold nanoparticle dimers and trimers for surface-enhanced Raman spectroscopy. *J. Am. Chem. Soc.* **2010,** *132* (31), pp 10903–10910.

8. Tao, A.; Kim, F.; Hess, C.; Goldberger, J.; He, R.; Sun, Y.; Xia, Y.; Yang, P., Langmuir−Blodgett Silver Nanowire Monolayers for Molecular Sensing Using Surface-Enhanced Raman Spectroscopy. *Nano Lett.* **2003,** *3* (9), pp 1229–1233.

9. Jackson, J.B.; Halas, N.J., Surface-enhanced Raman scattering on tunable plasmonic nanoparticle substrates. *Proceedings of the National Academy of Sciences* **2004,** *101* (52), pp 17930–17935.

10. Schwartzberg, A.M.; Grant, C.D.; Wolcott, A.; Talley, C.E.; Huser, T.R.; Bogomolni, R.; Zhang, J.Z., Unique Gold Nanoparticle Aggregates as a Highly Active Surface-Enhanced Raman Scattering Substrate. *J. Phys. Chem. B.* **2004,** *108* (50), pp 19191–19197.

11. Le Ru, E.C.; Blackie, E.; Meyer, M.; Etchegoin, P.G., Surface Enhanced Raman Scattering Enhancement Factors: A Comprehensive Study. *J. Phys. Chem. C.* **2007,** *111* (37), pp 13794–13803.

12. Kneipp, K.; Wang, Y.; Kneipp, H.; Perelman, L.T.; Itzkan, I.; Dasari, R.R.; Feld, M.S., Single Molecule Detection Using Surface-Enhanced Raman Scattering (SERS). *Phys. Rev. Lett.* **1997,** *78* (9), pp 1667–1670.

13. Andreou, C.; Hoonejani, M.R.; Barmi, M.R.; Moskovits, M.; Meinhart, C.D., Rapid detection of drugs of abuse in saliva using surface enhanced Raman spectroscopy and microfluidics. *ACS Nano.* **2013,** *7* (8), pp 7157–7164.

14. Piorek, B.D.; Andreou, C.; Moskovits, M.; Meinhart, C.D., Discrete Free-Surface Millifluidics for Rapid Capture and Analysis of Airborne Molecules Using Surface-Enhanced Raman Spectroscopy. *Anal. Chem.* **2014,** *86* (2), pp 1061–1066.

15. Pallaoro, A.; Hoonejani, M.R.; Braun, G.B.; Meinhart, C.D.; Moskovits, M., Rapid Identification by Surface-Enhanced Raman Spectroscopy of Cancer Cells at Low Concentrations Flowing in a Microfluidic Channel. *ACS Nano.* **2015,** *9* (4), pp 4328–4336.

16. Wang, C.; Yu, C., Analytical characterization using surface-enhanced Raman scattering (SERS) and microfluidic sampling. *Nanotechnology.* **2015,** *26* (9), p 092001.

17. Drummer, O.H., Drug testing in oral fluid. *Clin Biochem Rev.* **2006,** *27* (3), pp 147–159.

18. Huestis, M.A.; Cone, E.J., Methamphetamine disposition in oral fluid, plasma, and urine. *Ann. N. Y. Acad. Sci.* **2007,** *1098*, pp 104–121.

19. Allen, K.R., Screening for drugs of abuse: which matrix, oral fluid or urine? *Ann. Clin. Biochem.* **2011,** *48* (Pt 6), pp 531–541.

20. Engblom, C.; Gunnar, T.; Rantanen, A.; Lillsunde, P., Driving under the influence of drugs--amphetamine concentrations in oral fluid and whole blood samples. *J. Anal. Toxicol.* **2007,** *31* (5), pp 276–280.

21. Pethig, R., Review article-dielectrophoresis: status of the theory, technology, and applications. *Biomicrofluidics.* **2010,** *4* (2), p 022811.

22. Cetin, B.; Li, D., Dielectrophoresis in microfluidics technology. *Electrophoresis.* **2011,** *32* (18), pp 2410–2427.

23. Li, M.; Li, W.H.; Zhang, J.; Alici, G.; Wen, W., A review of microfabrication techniques and dielectrophoretic microdevices for particle manipulation and separation. *J. Phys. D: Appl. Phys.* **2014,** *47* (6), p 29.

24. Chrimes, A.F.; Kayani, A.A.; Khoshmanesh, K.; Stoddart, P.R.; Mulvaney, P.; Mitchell, A.; Kalantar-Zadeh, K., Dielectrophoresis-Raman spectroscopy system for analysing suspended nanoparticles. *Lab Chip.* **2011,** *11* (5), pp 921–928.

25. Chrimes, A.F.; Khoshmanesh, K.; Stoddart, P.R.; Kayani, A.A.; Mitchell, A.; Daima, H.; Bansal, V.; Kalantar-zadeh, K., Active control of silver nanoparticles spacing using dielectrophoresis for surface-enhanced Raman scattering. *Anal. Chem.* **2012,** *84* (9), pp 4029–4035.

26. Chrimes, A.F.; Khoshmanesh, K.; Tang, S.Y.; Wood, B.R.; Stoddart, P.R.; Collins, S.S.; Mitchell, A.; Kalantar-zadeh, K., In situ SERS probing of nano-silver coated individual yeast cells. *Biosens. Bioelectron.* **2013,** *49*, pp 536–541.

27. Cherukulappurath, S.; Lee, S.H.; Campos, A.; Haynes, C.L.; Oh, S.-H., Rapid and Sensitive in Situ SERS Detection Using Dielectrophoresis. *Chem. Mater.* **2014,** *26* (7), pp 2445–2452.

28. Cheng, I.F.; Chen, T.Y.; Lu, R.J.; Wu, H.W., Rapid identification of bacteria utilizing amplified dielectrophoretic force-assisted nanoparticle-induced surface-enhanced Raman spectroscopy. *Nanoscale Res. Lett.* **2014,** *9* (1), p 324.

29. Cheng, I.F.; Lin, C.C.; Lin, D.Y.; Chang, H.C., A dielectrophoretic chip with a roughened metal surface for on-chip surface-enhanced Raman scattering analysis of bacteria. *Biomicrofluidics.* **2010,** *4* (3).

30. Lin, H.Y.; Huang, C.H.; Hsieh, W.H.; Liu, L.H.; Lin, Y.C.; Chu, C.C.; Wang, S.T.; Kuo, I.T.; Chau, L.K.; Yang, C.Y., On-line SERS detection of single bacterium using novel SERS nanoprobes and a microfluidic dielectrophoresis device. *Small (Weinheim an der Bergstrasse, Germany)* **2014,** *10* (22), pp 4700–4710.

31. Almeida, G.B.; Poppi, R.J.; da Silva, J.A., Trapping of Au nanoparticles in a microfluidic device using dielectrophoresis for surface enhanced Raman spectroscopy. *Analyst.* **2017,** *142* (2), pp 375–379.

32. Jahn, I.J.; Zukovskaja, O.; Zheng, X.S.; Weber, K.; Bocklitz, T.W.; Cialla-May, D.; Popp, J., Surface-enhanced Raman spectroscopy and microfluidic platforms: challenges, solutions and potential applications. *Analyst* **2017,** *142* (7), pp 1022–1047.

33. Salemmilani, R.; Piorek, B.D.; Mirsafavi, R.Y.; Fountain, A.W., 3rd; Moskovits, M.; Meinhart, C.D., Dielectrophoretic Nanoparticle Aggregation for On-Demand Surface Enhanced Raman Spectroscopy Analysis. *Anal. Chem.* **2018,** *90* (13), pp 7930–7936.

34. Farquharson, S.; Shende, C.; Sengupta, A.; Huang, H.; Inscore, F., Rapid detection and identification of overdose drugs in saliva by surface-enhanced Raman scattering using fused gold colloids. *Pharmaceutics.* **2011,** *3* (3), pp 425–439.

35. Inscore, F.; Shende, C.; Sengupta, A.; Huang, H.; Farquharson, S., Detection of drugs of abuse in saliva by surface-enhanced Raman spectroscopy (SERS). *Appl. Spectrosc.* **2011,** *65* (9), pp 1004–1008.

36. Piorek, B.D.; Andreou, C.; Moskovits, M.; Meinhart, C.D., Discrete Free-Surface Millifluidics for Rapid Capture and Analysis of Airborne Molecules Using Surface-Enhanced Raman Spectroscopy. *Anal. Chem.* **2014,** *86* (2), pp 1061–1066.

37. Ackermann, K.R.; Henkel, T.; Popp, J., Quantitative online detection of low-concentrated drugs via a SERS microfluidic system. *ChemPhysChem.* **2007,** *8* (18), pp 2665–2670.

38. Haynes, C.L.; McFarland, A.D.; Van Duyne, R.P., Surface-Enhanced Raman Spectroscopy. *Anal. Chem.* **2005,** *77* (17), pp 338 A–346 A.

39. Kerker, M.; Siiman, O.; Bumm, L.A.; Wang, D.S., Surface enhanced Raman scattering (SERS) of citrate ion adsorbed on colloidal silver. *Appl. Opt.* **1980,** *19* (19), pp 3253–3255.

40. Li, W.; Zhao, X.; Yi, Z.; Glushenkov, A.M.; Kong, L., Plasmonic substrates for surface enhanced Raman scattering. *Anal. Chim. Acta.* **2017,** *984*, pp 19–41.

41. Wustholz, K.L.; Henry, A.I.; McMahon, J.M.; Freeman, R.G.; Valley, N.; Piotti, M.E.; Natan, M.J.; Schatz, G.C.; Van Duyne, R.P., Structure-activity relationships in gold nanoparticle dimers and trimers for surface-enhanced Raman spectroscopy. *J. Am. Chem. Soc.* **2010,** *132* (31), pp 10903–10910.

42. Munro, C.H.; Smith, W.E.; Garner, M.; Clarkson, J.; White, P.C., Characterization of the Surface of a Citrate-Reduced Colloid Optimized for Use as a Substrate for Surface-Enhanced Resonance Raman Scattering. *Langmuir.* **1995,** *11* (10), pp 3712–3720.

43. Bastús, N.G.; Merkoçi, F.; Piella, J.; Puntes, V., Synthesis of Highly Monodisperse Citrate-Stabilized Silver Nanoparticles of up to 200 nm: Kinetic Control and Catalytic Properties. *Chem. Mater.* **2014,** *26* (9), pp 2836–2846.

44. Mirsafavi, R.Y.; Lai, K.; Kline, N.D.; Fountain, A.W.; Meinhart, C.D.; Moskovits, M., Detection of Papaverine for the Possible Identification of Illicit Opium Cultivation. *Anal. Chem.* **2017,** *89* (3), pp 1684–1688.

ACRONYMS AND ABBREVIATIONS

CLS	classical least squares
DEP	dielectrophoresis
DEP-SERS	dielectrophoresis-surface-enhanced Raman spectroscopy
GC-MS	gas chromatography-mass spectroscopy
HPLC-MS	high-performance liquid chromatography-mass spectroscopy
IR	infrared
LSPR	localized surface plasmon resonances
MEMS	microelectromechanical systems
PC	principal component
PCA	principal component analysis
PDMS	polydimethylsiloxane
PVP	polyvinylpyrrolidone
SERS	surface-enhanced Raman spectroscopy
TERS	tip-enhanced Raman spectroscopy

DISTRIBUTION LIST

The following individuals and organizations were provided with one Adobe portable document format (pdf) electronic version of this report:

U.S. Army Edgewood Chemical
Biological Center (ECBC)
Senior Technologist Office
RDCB-DR
ATTN: Fountain, A.W. III

ECBC Technical Library
RDCB-DRB-BL
ATTN: Foppiano, S.
Stein, J.

Defense Technical Information Center
ATTN: DTIC OA


EDGEWOOD CHEMICAL BIOLOGICAL CENTER
A U.S. Army RDECOM Laboratory